Monthly Notices of the ROYAL ASTRONOMICAL SOCIETY

MNRAS **547,** 1–22 (2026) https://doi.org/10.1093/mnras/stag266
Advance Access publication 2026 March 27

Diversity of SEDs among the star-forming regions in NGC 1365

Stephen Hannon [1★] Eva Schinnerer [1] Bradley C. Whitmore [2] Hamid Hassani [3] Daizhong Liu [4] David A. Thilker [5] Jessica Sutter [6] Janice C. Lee [2] Jimena Rodriguez [2,7,8] Thomas G. Williams [9] Médéric Boquien [10] Daniel A. Dale [11] Erik Rosolowsky [3] Ralf S. Klessen [12,13] Aida Wofford [14,15] Kiana F. Henny [11] Kathryn Grasha [16,17] Rémy Indebetouw [18,19] and Kathryn Kreckel [20] the PHANGS team

Affiliations are listed at the end of the paper

Accepted 2025 December 22. Received 2025 November 23; in original form 2025 May 14

ABSTRACT

Studying samples of young star-forming regions allows us to statistically examine the evolution of their natal gas and dust along with the associated time-scales in the volatile early stages of their lives. With the Physics at High Angular resolution in Nearby GalaxieS survey data, we analyse the diversity of spectral energy distributions (SEDs) for the rich sample of massive star-forming regions found in NGC 1365. By combining unique detections across a variety of data sets from *Hubble Space Telescope (HST)*, *James Web Space Telescope (JWST)*, and Atacama Large Millimeter/sub-millimeter Array (ALMA) images, we produce a catalogue of 85 star-forming regions located in the central starbursting region of NGC 1365. Prior to analysis, we observe clear saturation effects in our four *JWST* Mid-Infrared Instrument (MIRI) images, and implement a saturation-correction method which allows us to recover data for 23 of 32 saturation-affected regions in these images. We then perform photometry in 13 *HST* & *JWST* images which are convolved to match the resolution of MIRI/F2100W ($\sim$64 pc), allowing us to probe star clusters as well as their immediate surroundings. Upon deriving their properties from SED-fitting using Code Investigating GALaxy Emission, we observe that regions selected with progressively redder wavebands are younger and generally more reddened. We also identify three SED features correlated with age: (1) sources with a positive near-infrared slope [(F300W + F360M)/(2×F200W)] are by median half the age of those with negative near-infrared slopes; turnover occurs around 6 Myr, (2) the relative strength of dust emission (F2100W/F200W), and (3) polycyclic aromatic hydrocarbon emission (F335M/F300M) both show that larger such ratios correlate with younger ages. Considering our working resolution, these features are robust to the inclusion of nearby emission surrounding star clusters.

Key words: galaxies: star clusters: general – galaxies: individual: NGC 1365.

1 INTRODUCTION

Understanding the earliest stages of stellar evolution and the evolution of the gas and dust from which these stars are born is critical to accurately modelling the complete star formation cycle in galaxies. *Hubble Space Telescope (HST)* has aided in the discovery that young ($\leq$100 Myr), massive ($\geq 10^4$ $M_\odot$) star clusters, which represent fundamental building blocks of galaxies (S. F. Portegies Zwart, S. L. W. McMillan & M. Gieles 2010), are forming in merging and starbursting galaxies (e.g. J. A. Holtzman et al. 1992; B. C. Whitmore et al. 1993; R. W. O'Connell, I. Gallagher & D. A. Hunter 1994; A. J. Barth et al. 1995), and provide insight into the conditions required to form massive clusters. This includes dusty regions where stars are formed within giant molecular clouds (GMCs; C. J. Lada & E. A. Lada 2003), which is also observed in luminous infrared galaxies (e.g. A. Adamo et al. 2020; S. T. Linden et al. 2021).

With the advent of *James Web Space Telescope* (*JWST)* and its resolution down to $\sim$0.06 arcsec, we are now capable of probing the properties of embedded star formation at the cluster scale in galaxies up to $D \sim 20$ Mpc. Physics at High Angular resolution in Nearby GalaxieS (PHANGS;[1] see PHANGS-ALMA, A. K. Leroy et al. 2021; PHANGS-MUSE, E. Emsellem et al. 2022; PHANGS-*HST*, J. C. Lee et al. 2022; PHANGS-*JWST*, J. C. Lee et al. 2023; PHANGS-*AstroSat*, H. Hassani et al. 2024) is one of the newest and largest extragalactic surveys to systematically study these topics, addressing the complete star formation cycle on the cluster scale across a broad range of galactic environments.

NGC 1365 is one such nearby galaxy at a distance 19.6 Mpc (G. S. Anand et al. 2021a, b), at which *JWST*'s resolution in the *F2100W* band ($\sim$0.67 arcsec) represents a physical scale of

★ E-mail: hannon@mpia.de

[1] https://www.phangs.org

∼64 pc. It is a popular target both due to its proximity and high rate of star formation as a dusty, barred spiral galaxy. In the PHANGS sample, NGC 1365 was one of the first targets observed with *JWST* (J. C. Lee et al. 2023), and its star cluster sample has been studied across a broad range of wavelengths, including *HST*-selected studies (e.g. B. C. Whitmore et al. 2023), PAH-selected studies (polycyclic aromatic hydrocarbons; e.g. M. J. Rodríguez et al. 2023; B. C. Whitmore et al. 2023) as well as 10- and 21 μm-selected studies (e.g. E. Schinnerer et al. 2023 or H. Hassani et al. 2023, respectively). These studies, among others, are part of the PHANGS-*HST*, PHANGS-*JWST*, and PHANGS-ALMA programmes.

The general star formation process begins with an overdensity of cold, molecular gas (e.g. C. J. Lada & E. A. Lada 2003). Within these clouds, there are regions that gravitationally coalesce and ultimately reach the requisite volume densities to form new stars. The radiation pressure, stellar winds, and eventual supernovae from these newly formed massive stars then disrupt and disperse the remaining birth material on a relatively short time-scale (within a few Myr; see E. Schinnerer & A. K. Leroy 2024 for a review). The aim of this study is to combine the information gained across the aforementioned uniquely selected catalogues in order to glean information about how we interpret the spectral energy distributions (SEDs) of young, dusty star clusters, which may still be embedded in their surrounding interstellar medium (ISM) reservoir, from a variety of source selections. As a prime example, we focus on the central region of NGC 1365.

To this end, a growing number of studies have begun to uncover features with which we associate the youngest stages of a stellar population. *HST*-based studies have used evolutionary characteristics of HII regions using Hα emission as well as the cluster SEDs (e.g. B. C. Whitmore et al. 2011; K. Hollyhead et al. 2015; S. Hannon et al. 2019, 2022; M. Messa et al. 2021; S. Deshmukh et al. 2024), to determine that the clearing of gas takes place prior to the onset of supernovae, in agreement with ALMA-based studies of GMCs by CO detection (e.g. K. Grasha et al. 2018, 2019; A. M. Matthews et al. 2018; J. Kim et al. 2021). Studies such as M. Messa et al. (2021) & S. T. Linden et al. (2024) have expanded these analyses to include Near Infrared Camera (NIRCam) observations, also finding evidence of pre-supernova clearing, although T. McQuaid et al. (2024) has found this feature to be dependent on cluster mass. M. Messa et al. (2021) also observed very short clearing time-scales, on order of 1 Myr, roughly in agreement with *HST*-based studies (e.g. S. Hannon et al. 2022).

PAHs, which are observable in *JWST*'s 3.3, 7.7, and 11.3 μm filters, offer a promising interstellar dust tracer, and have been used to characterize the content of interstellar dust (e.g. B. T. Draine 2003; A. G. G. M. Tielens 2008; A. Li 2020). Their relative fractions allow us to derive more information, including the charge and size of the PAH population (J. D. T. Smith et al. 2007; T. S. Y. Lai et al. 2020; B. T. Draine et al. 2021). The characteristics of PAH emission can not only help us identify some of the youngest, dustiest star clusters (M. J. Rodríguez et al. 2023), but also allow us to gather information regarding the age of the host star clusters via the flux ratios of different PAH emission features (e.g. D. A. Dale et al. 2023; K. M. Sandstrom et al. 2023). Furthermore, studies such as A. Pedrini et al. (2024) & A. Knutas et al. (2025) found a correlation between PAH morphology and cluster age, where embedded clusters, evidenced by compact emission, are younger than their exposed counterparts, and the time-scale for such emergence is around 5–7 Myr.

In addition to PAHs, larger dust grains also prove to have a central role in shaping the radiation field in galaxies by converting short-wavelength light from stars and other emitters into long-wavelength emission in the infrared (F. Galliano, M. Galametz & A. P. Jones 2018). Massive, embedded stars create strong radiation fields that heat nearby dust so that the mid-infrared (IR) can be used as a tracer for star formation (D. Calzetti et al. 2007; R. C. Kennicutt & N. J. Evans 2012). Studies such as H. Hassani et al. (2023) have leveraged this to identify embedded, compact sources which are coincident with stellar structures using the 21 μm waveband. Beyond the mid-IR, super star clusters which are deeply embedded within their natal gas have been identified and studied using ALMA [sub-]millimeter continuum observations (e.g. K. E. Johnson et al. 2018; R. C. Levy et al. 2022). Some of these embedded clusters represent precursors to the ancient globular clusters ubiquitous across massive galaxies and can have a major impact on the surrounding ISM (W. E. Harris 2003).

All of these discoveries continue to inform and improve the models we use for the earliest stages of stellar evolution (e.g. M. Boquien et al. 2019; B. T. Draine et al. 2021). By collecting the information gained across a broad range of wavelengths, this study seeks with a larger scope to examine and compare the properties of star clusters as well as their immediate surroundings, identified with various instruments, in order to continue disentangling the characteristics of star-forming (SF) regions both in their infancy and as they evolutionarily progress. Furthermore, we seek to test the robustness of these properties and characteristics with commonly resolved images to match the lowest resolution observations in our study (∼64 pc).

This paper is organized as follows. Section 2 first provides an overview of the data utilized in this study, which is comprised of *HST*, *JWST*, and ALMA images as well as the source detection method used for each instrument, and also provides a method to address the saturation effects observed in particular in our MIRI images prior to the convolution of our images and subsequent photometry. To conclude the section, we detail the SED-fitting procedure employed to derive characteristic properties of our sample of star-forming (SF) regions. Section 3 begins the analysis of the SED-fitting results, which include a comparison of the statistical properties of the sources based on selection method, as well as the quality of the the fits. Section 4 entails a discussion of the primary features of SEDs correlated with age, and also includes comparison of central versus non-central sources selected with F2100W. Section 5 lastly provides a summary of our work.

2 DATA

The focus of this analysis is on the central starbursting region of NGC 1365, a nearby ($D = 19.6$ Mpc, 1 arcsec $\approx$ 95 pc; G. S. Anand et al. 2021a, b), grand-design, barred spiral galaxy (type SB(s)b; G. Vaucouleurs et al. 1991), which hosts an active galactic nucleus (R. Morganti et al. 1999) and has the highest star formation rate (SFR) in the PHANGS–ALMA sample ($\log_{10}$(SFR) = 1.24 $M_\odot$ yr^{-1}; A. K. Leroy et al. 2021). With the available PHANGS data, we are able to examine data across multiple instruments, namely *HST* (J. C. Lee et al. 2022), which includes *NUV*, *U*, *B*, *V*, and *I* broad-band images, *JWST* (J. C. Lee et al. 2023), which includes both NIRCam images (F200W, F300M, F335M, F360M) and MIRI images (F770W, F1000W, F1130W, F2100W), as well as ALMA [sub-]millimeter continuum maps (A. K. Leroy et al. 2021), which include the 0.87 and 1.3 mm wavebands (D. Liu et al. 2023; E. Schinnerer et al. 2023). We note that hereafter, we may refer to

these bands with their pivot wavelength instead (e.g. 2, 10, 21 μm); however this is for simplicity and not because they have been further processed. From this sample of 15 images, we compile a catalogue based on source detections across multiple filters and instruments. Footprints of each of the data sets are overlaid on a 10 arcmin × 10 arcmin digitized sky survey image in Fig. A1 for reference.

2.1 Sample of massive star-forming regions

For the generation of a sample of massive star-forming regions, we mostly rely on existing catalogues from the literature. To create our own catalogue of objects for analysis, we start with B. C. Whitmore et al. (2023), who built their sample of star clusters in NGC 1365 beginning with identifying 19 optically selected clusters (selected to be brighter than 26.0 mag in *HSTB*, *V*, and *I* bands), which had modelled ages less than 10 Myr, and modelled masses greater than 10^6 $M_\odot$ (J. A. Turner et al. 2021; B. C. Whitmore et al. 2021). They then add 16 new, partly or heavily embedded massive young objects that are selected to be brighter than 20.0 mag in at least two PAH filters (*F335M*, *F770W*, *F1130W*) as well as the *F200W* filter. These sources, which were not found in the original *HST* catalogue, will be referred to as PAH-selected sources. B. C. Whitmore et al. (2023) also add two young, massive objects to their catalogue, which were identified in radio continuum images (A. Sandqvist, S. Jorsater & P. O. Lindblad 1982; 1995) and are heavily saturated in *F770W*, however we will focus on the larger samples of objects in this work, and thus omit these two radio-identified sources. This leaves us with 19 *HST*-selected and 16 PAH-selected sources.

Secondly, we add objects from H. Hassani et al. (2023), who identify bright, compact sources in *JWST*/MIRI's *F2100W* filter using the ASTRODENDRO software package (T. Robitaille et al. 2019). This method was chosen over more-typical point source identification algorithms due to the ISM-tracing nature of the 21 μm data, which can cause even compact sources to have irregular morphologies. As a result, H. Hassani et al. (2023) identified 367 compact 21 μm sources in NGC 1365 which have a ratio of peak surface brightness-to-background that is greater than 5. From those 367 sources, we filter them to have fluxes of $F_{10\mu m} > 100$ μJy and $F_{21\mu m} > 200$ μJy to represent a more massive sample, leaving us with 16 sources identified with *F2100W*. In addition to these 16 sources in the centre of NGC 1365, H. Hassani et al. (2023) also identified 23 sources in the *F2100W* filter which are located outside of the central, starbursting region of the galaxy. These non-central sources are excluded from our primary analysis, however we examine them in a separate, comparative analysis in Section 4.2.

Using the same selection methodology of H. Hassani et al. (2023), E. Schinnerer et al. (2023) identify compact objects in *JWST*/MIRI's F1000W image. Upon applying the same brightness criteria ($F_{10\mu m} > 100$ μJy and $F_{21\mu m} > 200$ μJy), 38 additional 10 μm sources in the central region of NGC 1365 are added to our catalogue.

Lastly, we include sources identified with Atacama Large Millimeter/submillimeter Array (ALMA) continuum images at wavelengths of 0.87 and 1.3 mm. To identify these sources, we first use the Python Blob Detector and Source Finder (N. Mohan & D. Rafferty 2015) to decompose each image into a set of Gaussians. By doing so, we detected a total of 109 and 34 potential sources in the 0.87 and 1.3 mm images, respectively. In order to remove spurious sources from these ALMA catalogues, we take each image and multiply each pixel value by −1 and rerun the source detection algorithm. With this method, we assume the noise properties of the negative 'sources' are similar to the true sources and thus treat the negative image as an empty image to determine a signal-to-noise (S/N) threshold. Upon doing so, we find these negative 'sources' are detected up to an S/N of 3.6, and as such we require our reliable sources to have greater S/N than that threshold. After the removal of those lower S/N sources, we are left with 33 and 19 sources across the 0.87 and 1.3 mm images, respectively, for a total of 48 sources identified with ALMA. 16 of these sources are shared between the two ALMA images, while the 0.87 and 1.3 mm images individually produce 17 and 3 unique source detections, respectively, for a total of 36 ALMA sources. The varied detection numbers stem from differing resolutions (∼0.09 arcsec for 0.87 mm and ∼0.25 arcsec for 1.3 mm), as well as the 0.87 mm image having a relatively smaller background RMS.

With 19 *HST*-selected sources, 16 PAH-selected sources, 38 10 μm-selected sources, 16 21 μm-selected sources, and 36 ALMA-selected sources, we have a total of 125 sources in our catalogue of central NGC 1365 objects. The final step we take in the production of our working catalogue is to find and remove duplicate sources across the four catalogues. To do so, we identify all objects that have a neighbouring source within the PSF of *JWST*/MIRI's *F2100W* filter (FWHM ≈ 0.67 arcsec). From this search, we find that 40 of our sources are within the *F2100W*'s PSF of another source. To select the best centre for these matched objects, we examine the different positions in each of the bands to check for reasonable source matching, and generally choose the coordinates of the object with the greatest S/N in its detected band, or in the case of comparable S/Ns, the coordinates corresponding to the image with the highest native resolution. Given the eventual working resolution of this study (0.67 arcsec; Section 2.3), it is important to note that we are in fact analysing both clusters and their immediate surroundings, and thus we will hereafter refer to our sample as star-forming regions (SF regions) in this work, or simply just sources.

Considering that 40 of the aforementioned 125 sources are duplicates, our final catalogue consists of 85 unique SF regions located in the centre of NGC 1365. Of these 85 central SF regions, 12 are specifically unique to the B. C. Whitmore et al. (2023) *HST* & PAH catalogue (there are no objects identified only in *HST* and not in any PAH bands, and vice versa), and were not identified in any of the 10, 21 μm, or ALMA catalogues. This means that there are 7 *HST*- and 4 PAH-selected sources which were also selected in at least one of the other three catalogues. Here we remind the reader that different literature catalogues have different flux limits imposed for their selection bands, and so a source not being present in a certain catalogue does not necessarily imply a non-detection in other bands. To this end, H. Hassani et al. (2025) identified 50 per cent completeness limits to be 4 and 21 μJy for *F1000W* and *F2100W* sources, respectively, in NGC 1365. With that in mind, 10 of 12 regions unique to the B. C. Whitmore et al. (2023) catalogues were detected in at least 2 of the *HST* filters, and the other two regions were not detected beyond the *F770W* PAH filter. Thus it is somewhat reasonable that these sources were not selected in *F1000W* and beyond.

Similarly there are 9, 8, and 14 sources unique to the 10 μm, central 21 μm, and ALMA catalogues, respectively. This also means that 29 10 μm sources, 8 10 μm sources, and 22 ALMA sources are identified in at least one other catalogue. All informa-

Table 1. An abbreviated table of information for the sources examined in this study, including IDs, filters in which the objects are detected (see Section 2.1), photometry (Section 2.4), and SED-fit properties (Section 2.5). Photometry and SED-fitting results have been rounded in this abbreviated table; the fully precise measurements are provided in the full table, which is provided as a Supplementary File with this work.

ID	RA	Dec.	B	...	$F_{\rm N}$	$F_{\rm N,err}$	...	Age (Myr)	$E(B-V)$ (mag)	Mass (10^5 $M_\odot$)	χ^2
1	53.400281	−36.142577	0	...	0.000 25	0.000 17	...	3.8	2.50	29	1.1
2	53.399891	−36.142575	1	...	0.000 82	0.000 10	...	5.1	0.88	6.2	1.3
3	53.399386	−36.142085	1	...	0.002 18	0.000 18	...	2.8	0.88	8.4	1.9
.	.	.	.	...	.	.	...	.	.	.	.
.	.	.	.	...	.	.	...	.	.	.	.

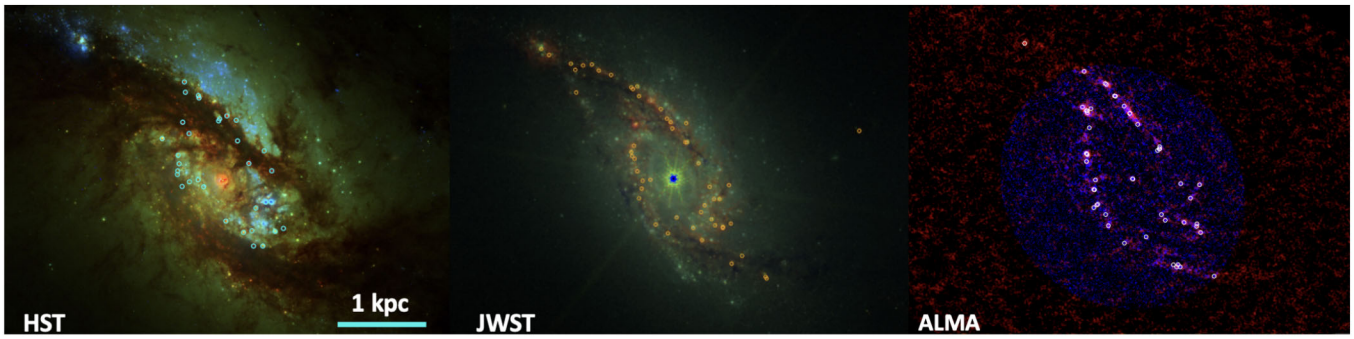

Figure 1. RGB images comparing *HST*/UVIS (left) and *JWST*/NIRCam (middle), and ALMA (right), each convolved to the resolution of the *F2100W* filter (0.67 arcsec), for the central region (∼ 5 kpc) of NGC 1365. For the *HST* image, B = F275W + F336W, G = F438W + F555W, and R = F814W; for the *JWST* image, B = F200W, G = F300M, and R = F335M; for the ALMA image, B = 0.87 mm, R = 1.3 mm. The blue circles (left panel) indicate sources which are identified with *HST* (B, V, I bands) while the orange (middle panel) and white (right panel) circles indicate sources which are identified with *JWST* (F1000W & F2100W) and ALMA (0.87 & 1.3 mm), respectively. A 1 kpc scale bar is provided for reference.

tion regarding with which filters each source has been identified, along with coordinates, photometry (Section 2.4), and SED-fit properties (Section 2.5) are provided in a Supplementary Table with this work, and an abbreviated version of this table is shown in Table 1. We note here that each of the objects identified in multiple catalogues will be included in the subsequent analysis of each respective catalogue of sources, and the uniquely identified sources are also examined separately.

To highlight the importance of source detection beyond *HST*, Fig. 1 displays our sample of objects in the central region of NGC 1365 which are identified with *HST* (blue circles), *JWST* (orange circles), and ALMA (white circles), along with composite false-colour images of *HST* bands (left), *JWST* bands (middle), and ALMA bands (right).

2.2 Saturation corrections

The *JWST* images used in this study have been processed with the pipeline setup by the PHANGS-*JWST* team (T. G. Williams et al. 2024). For the central region of NGC 1365 in particular, there are massive objects which appear heavily saturated in the MIRI filters, where the saturation becomes increasingly more evident from *F770W* to *F2100W*.

For the three sources displayed in Fig. 2, there are three observable saturation effects. First, the central pixels, which saturate almost immediately, are properly flagged by the pipeline and discarded as NaN values. Fig. 3 shows how the signal accumulates across the individual observational frames (i.e. ramps) for various sources (based on their central pixel), and these highly saturated objects are at or nearly capped at ∼60 000 DNs from the very first frame (shown as the red lines in Fig. 3). Beyond those central pixels, we see similar effects to 'snowballs', where the signal from saturated pixels floods into adjacent pixels.[2] One of these resultant effects is the relative depressions in signal surrounding parts of the saturated pixels. These pixels, while not immediately saturated themselves, were likely flagged as having 'jumps' when the signal from the primary saturated pixels spilled over into them. Photoelectrons may have then been temporarily trapped by small defects in the detector's pixels, leading to the observed below-expected count rates. The last effect observed in Fig. 2 is the extent of the 'halo', or the remaining brighter spots that are highlighted by the hexagonal shape found in the PSF of these images. These pixels have gone uncorrected because their count rates were below the pipeline's jump detection threshold.

We highlight a different set of saturated sources in the top row of images of Fig. 4. Here, the objects are not as bright as they are in Fig. 2, but they still saturate quickly (within four or five frames; shown as blue lines in Fig. 3), and display similar depressions as those found around the immediately saturated pixels of Fig. 2. In addition to the similar appearance, the ramps for these two types of depressed regions are closely matched, likely indicating a similar cause for the lower count rates.

In order to provide more accurate data for these regions, we have tried making two adaptations to our standard pipeline; the standard we use here is the official STScI PHANGS-*JWST* Pipeline (`PJPipe`; T. G. Williams et al. 2024). The first change we make to the pipeline addresses the MIRI first frame correction step.[3] In the default pipeline, this step flags the first frame of every

[2] https://jwst-docs.stsci.edu/known-issues-with-jwst-data/shower-and-snowball-artifacts
[3] https://jwst-pipeline.readthedocs.io/en/latest/jwst/firstframe/index.html

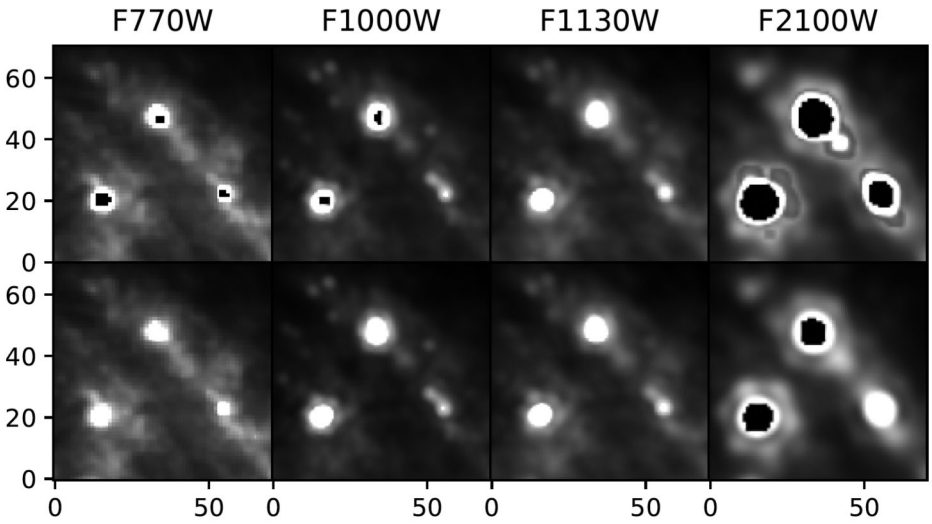

Figure 2. Examples of extremely saturated sources observed in NGC 1365 using *JWST*/MIRI. The original pipeline image is displayed in the top row while the RSCD-corrected version is shown in the bottom row. The black pixels in the centres of SF regions along top row represent NaN values, or complete saturation. In this cutout, three sources show saturation in F770W and are recovered with our correction. Similarly, two are saturated in *F1000W* and both are recovered, none of the sources are saturated in *F1130W*, and one of the three saturated sources are recovered in *F2100W*. The ramps used to determine the signal for each of these three sources are shown in Fig. 3.

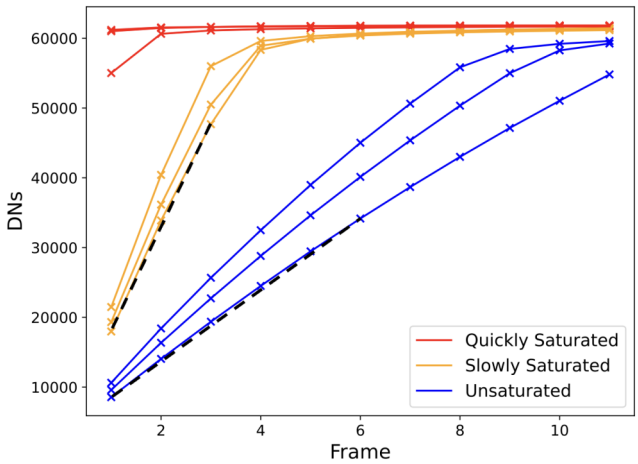

Figure 3. Accumulation of data across each frame (i.e. 'ramps') for three types of sources observed with the *F2100W* filter for NGC 1365: (i) Those that quickly saturate (the red lines denote the three sources highlighted in Fig. 2), (ii) those that saturate a bit more slowly (orange lines denote the three sources highlighted in Fig. 4), and (iii) sources which did not seem to be affected by saturation (blue lines). Straight dashed black lines are added along two of the ramps to emphasize the near-linearity across the first three frames for slowly saturated sources and the first several frames of unsaturated sources.

integration as 'do not use' (as long as the total number of frames is greater than three), in order to remove initial biases in the pixel, which are largely related to the resets right before the start of the integration. The second change is to the reset switch charge decay (RSCD) step.[4] MIRI detectors use a field effect transistor (FET) as a switch to allow charge to build up and to also clear the charge between each exposure. However, this reset by the FETs is not instantaneous and instead uses exponential adjustments, causing the initial frame(s) in an integration to be offset from their expected values. The RSCD step in the default pipeline therefore flags a number of frames after the first as 'do not use' as well. Normally, these steps are important in eliminating initial biases in an observation, but in the case of saturating pixels, it could be removing otherwise fine data points from the subsequent ramp fitting procedure, which is used to determine the average count rates. Thus, our experimental state of the pipeline will include the first frame and/or RSCD-flagged frames. We note that in creating our saturation-corrected versions of the pipeline, there is no anchoring to independent, non-*JWST* images after the corrections are made. After rigorous comparison between our modified images and the original pipeline images described in T. G. Williams et al. (2024), we continue to use the RSCD-corrected images as those result in a better recovery of low-signal emission and a better preservation of the PSF than the first frame + RSCD images. More details are provided in Appendix B.

As displayed in the Figs 2 and 4, MIRI's *F2100W* image of NGC 1365 is the most affected by saturation. Within the image, 32 of the 85 unique sources in our sample (38 per cent) are either completely saturated or are impacted by saturation effects (i.e. are in or around either the completely saturated sources or abnormally depressed regions). Based on the dimmest region where there are saturation effects, saturation appears to take place around peaks >2500 MJy sr^{-1}. Upon implementing our corrections for saturation, all sources initially affected are recoverable up to 10 000 MJy sr^{-1}. This means that all but three regions (containing nine unique sources), one of which is the galaxy centre, become recoverable, bringing our total number of saturated sources in *F2100W* to nine out of 85, or 11 per cent.

Similarly, we observe saturation effects in some of the same regions in the other MIRI filters (*F770W*, *F1000W*, *F1130W*). None of the photometry of the galaxy centre is recovered for each of these filters after our saturation corrections, as was the case with *F2100W*. However, for *F770W*, there are six other saturated sources which have been recovered, indicating a lower limit for

[4] https://jwst-pipeline.readthedocs.io/en/latest/jwst/rscd/description.html

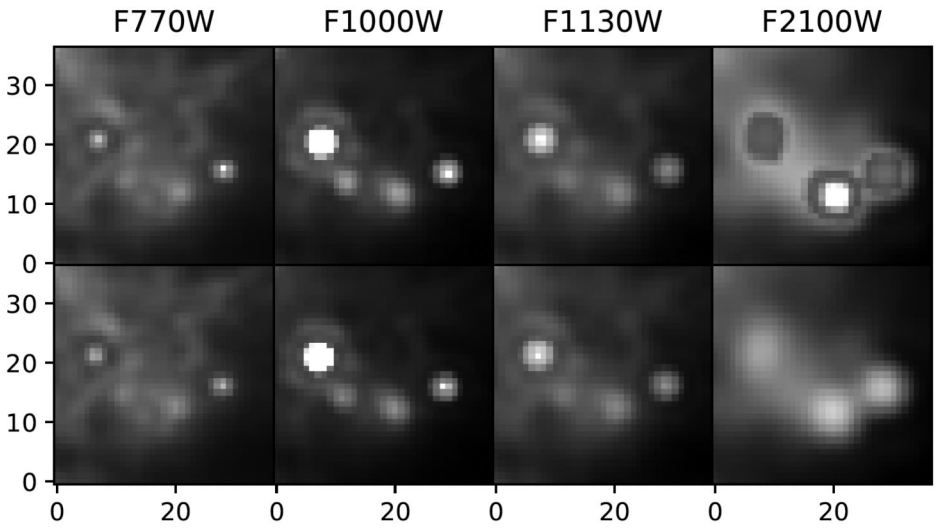

Figure 4. Other examples of saturation effects observed in the *JWST*/MIRI images of NGC 1365. The original pipeline image is displayed on top while the corrected version is shown on the bottom. Across the image, *F2100W* suffers the most from saturation effects, which is evident in the displayed region, as it is the only filter in which saturation effects are observed. These three sources have saturated more gradually than those observed in Fig. 2, causing the ramp-fitting procedure to underestimate the flux by discarding the first frame of the observation (see Fig. 3).

saturation at 1600 MJy sr^{-1} and an upper limit for recovery of 2000 MJy sr^{-1}. *F1000W* also shows six saturated sources besides the centre, all of which are recovered, corresponding to lower and upper limits of 1000 and 2800 MJy sr^{-1}, respectively. Lastly, *F1130W* contains six saturated sources other than the centre, however, all of these regions still show signs of saturation effects after our corrections are implemented. Based on the brightest unsaturated region and the dimmest saturated region, we note that saturation occurs in this filter between 1500 and 5000 MJy sr^{-1}, however there is no way to tell what the recoverable limit is with our saturation correction since none of the saturated sources are recovered.

Other works have explored the use of fitting an outer PSF in order to recover the photometry of saturated sources (e.g. D. Liu et al. 2023). While this may be viable for a small number of sources, we focus our attention in this work's analysis on the greater sample of objects we have at our disposal.

2.3 Convolution

After correcting for saturation and before performing photometry on our selection of sources, we convolve each of our images to a common resolution, matching that of *JWST*/MIRI's *F2100W* filter (PSF of 0.67 arcsec, or 64 pc). The convolution kernels are produced using `jwst kernels` (see also F. Belfiore et al. 2023), which follows the methodology of G. Aniano et al. (2011) and utilizes the *JWST* PSFs obtained with the WebbPSF tool (M. D. Perrin et al. 2014). Individual kernels are created for each of the *JWST* filters, while the *F200W*-to-*F2100W* kernel is used as an approximation to convolve each of the *HST* images. Lastly, the ALMA images are convolved with Common Astronomy Software Applications (CASA) *imsmooth* routine, using a Gaussian kernel with major and minor beam axes matching the 0.67 arcsec PSF of the *F2100W* filter. After convolving each of the images to the resolution of F2100W, we regrid them so that each of the images is also on the same pixel grid as *F2100W*. The original images are presented in the main body of the text in Fig. 5, while the corresponding convolved images are provided in Fig. A2 of Appendix A. Both images include the PSF displayed as a cyan circle in the lower left corner of each image. The ALMA images are only utilized for additional source detection. With this working resolution, we are not necessarily looking at individual star clusters, but more so SF regions.

2.4 Photometry

With all of the images convolved to the same resolution (0.67 arcsec), we perform photometry on each of our 15 images, all of which are converted to surface brightness units of MJy sr^{-1}. For each source, we sample the brightest local maximum in each image using the best centre (see Section 2.1) among our source catalogues (*HST*/PAH/Radio (B. C. Whitmore et al. 2023), 10 μm (E. Schinnerer et al. 2023), 21 μm (H. Hassani et al. 2023), and each of the ALMA images (0.87 and 1.3 mm). From this estimated peak in surface brightness, we subtract an estimate of the median background calculated in an annulus with radii between 2 and 3 times the width of the PSF (between 1.34 and 2.01 arcsec), as performed in H. Hassani et al. (2023).

From the background-subtracted peak surface brightness, we then multiply it by the solid angle subtended by the MIRI PSF in the *F2100W* band ($\Omega_{F2100W} = 1.61 \times 10^{-11}$ sr), as calculated using the models from the WebbPSF package (M. D. Perrin et al. 2014), in order to convert our measurements into flux densities (MJy) over a 0.67 arcsec-wide aperture. Considering this working resolution, it is important to examine how well-matched the photometry of our convolved SF regions are to the photometry of the regions at their native resolution. To this end, for example, we find that the median recovered flux of our convolved sources in *F200W* is ∼95 per cent that of the flux based on the image's native resolution when using the same aperture size.

We display the range of flux densities of the stellar continuum sampled at 2 μm in Fig. 6 for each of the five catalogues examined in this sample, where there is a consistent decline in flux from the objects selected from the bluer *HST* wavebands (me-

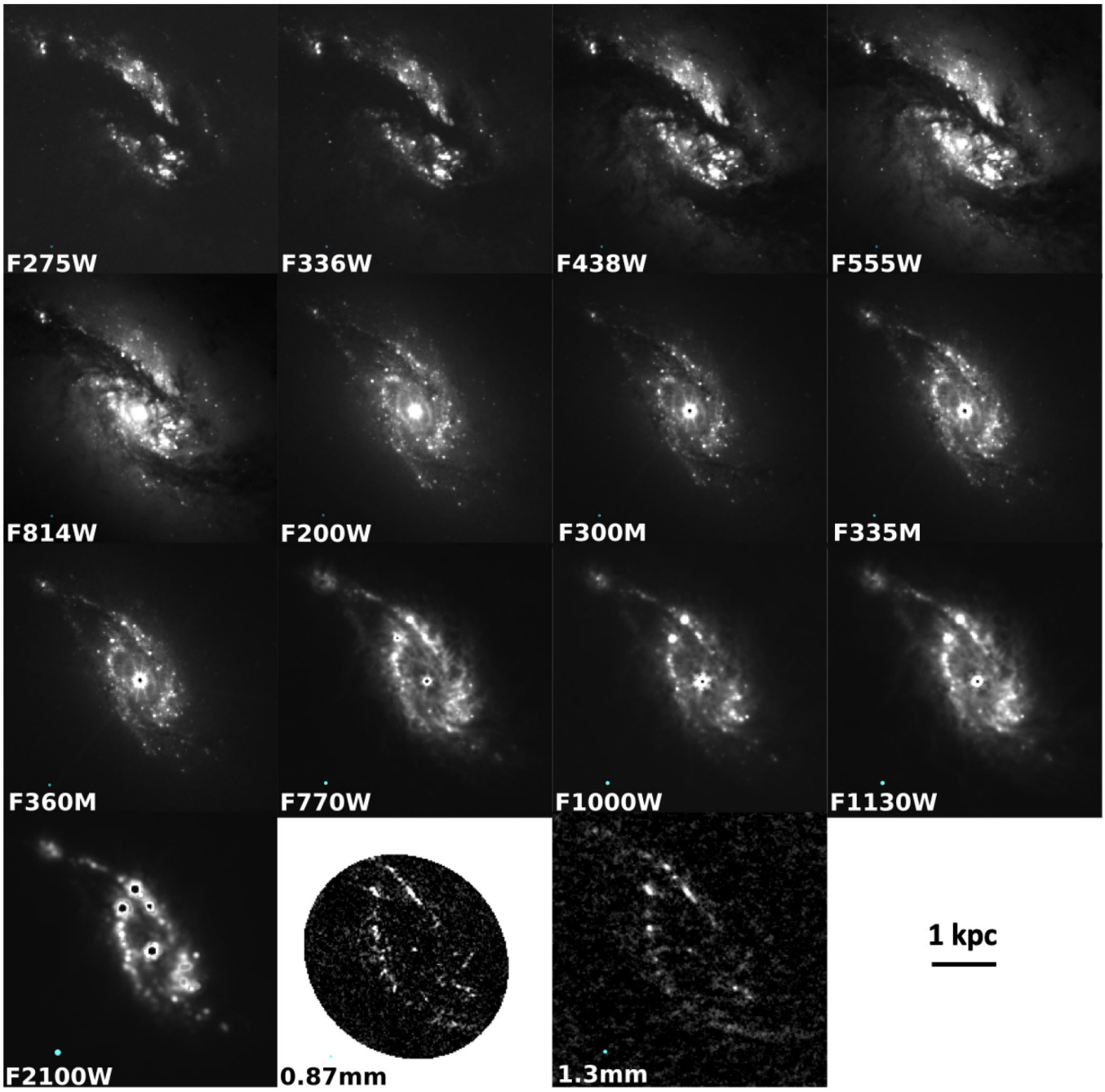

Figure 5. Complete sample of greyscale images for the central region of NGC 1365 (images are ∼4.5 kpc wide; 1 kpc scale bar is given in the bottom-right of the image for reference), observed with *HST*, *JWST*, and ALMA. Each of the images is presented here in its native resolution, while an equivalent figure with each of the images convolved to match the resolution of the MIRI *F2100W* filter (full width at half-maximum, FWHM of 0.67 arcsec) is shown in Appendix A. The filter name is labelled in the lower left of each image along with a cyan dot above the label representing the PSF for each filter).

dian $f_{\nu,2\mu m} = 0.51$ mJy) to the redder ALMA wavebands (median $f_{\nu,2\mu m} = 7.3 \times 10^{-3}$ mJy). We will identify resultant effects of this feature and others in the SEDs of our sample of SF regions in Section 4. Photometric uncertainties for each source are determined with the median absolute deviation in nearby background of each image, and are converted to match the area of the aperture.

Lastly, some of the objects have non-detections in some of the filters, e.g. non-detections in *HST* filters for the dustier sources identified in MIRI or ALMA images. For example, we find that 22 of our 38 *F1000W*-selected sources (58 per cent), 15 of our 16 central *F2100W*-selected sources (94 per cent), and 32 of our 36 ALMA-selected sources (89 per cent) are not detected in at least 2 *HST* bands. For such non-detections in a given filter, we opt to use upper limits based on the 1σ uncertainty in place of the original flux value. We remind the reader that all of our original photometry across all *HST*, NIRCam, and MIRI bands are provided as a Supplementary File with this work, and an abbreviated version is shown in Table 1.

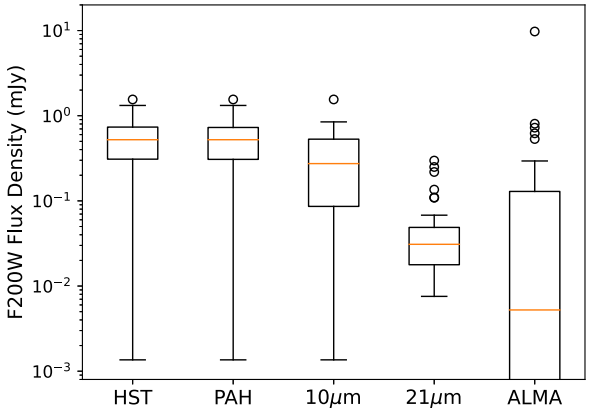

Figure 6. Box and whisker plots displaying the distributions of flux densities in *F200W* for SF regions according to the catalogue with which they were selected (*HST*, PAH, 10, 21 μm, or ALMA). Orange lines represent the medians, the edges of the boxes represent 25th and 75th percentiles, the whiskers extend from the box to 1.5× the interquartile range, and the circles represent the outliers. As SF regions are selected in redder bands, the flux density of the stellar continuum sampled at 2 μm decreases, from a median of ∼0.5 mJy for *HST*-selected sources down to ∼0.007 mJy for ALMA-selected sources.

2.5 SED fitting procedure

In order to characterize our sample of SF regions, we employ the Code Investigating GALaxy Emission (CIGALE; M. Boquien et al. 2019) to estimate their stellar properties including their age, mass, and reddening due to dust.

For the fitting procedure, we closely follow the parameters utilized by H. Hassani et al. (2023). Since we are using the lower resolution of *F2100W*, it is possible to have a diluted star formation history (SFH), and thus implement a double exponential star formation history with an e-folding time ranging from 0.01 to 10 Myr, and a late starburst with an e-folding time ranging from 0.001 to 0.1 Myr. Additionally, we allow the mass fraction of the late burst population to be 0, 0.1, or 0.5 with the age of the latest burst to be 1 Myr. Based on the characteristic time-scales for star formation in our galaxies, we consider a range of stellar population ages from 1 to 20 Myr. We also restrict our models to 0.0 mag $< E(B-V) <$ 3 mag in increments of 0.1, and we use an attenuation law from D. Calzetti et al. (2000). This reddening grid has been chosen based on PHANGS-MUSE maps (E. Emsellem et al. 2022), as well as providing the best fits for the SED modelling of our SF regions. We include B. T. Draine & A. Li (2007) and B. T. Draine et al. (2014) dust models, describing the fraction of the total dust mass exposed to a range of stellar intensities, and these models follow a power-law distribution from $U_{\rm min}$ to $U_{\rm max}$ with $\mathrm{d}M/\mathrm{d}U \propto U^{-\alpha}$. Since individual HII regions can have intense radiation fields, we consider $0.5 < U_{\rm min}/U_0 < 50$, where $U_{\rm min}$ is the parameter from B. T. Draine & A. Li (2007) that characterizes the interstellar radiation field (ISRF) and U_0 is the ISRF in the solar neighbourhood (J. S. Mathis, P. G. Mezger & N. Panagia 1983). We consider a fraction of the dust mass heated by the power-law distribution of radiation fields with intensity up to $U_{\rm max} = 10^7\,U_0$ with an illuminated fraction of $\gamma = 0.5, 1.0$, which is similar to the findings of J. Chastenet et al. (2019) in the LMC, and we allow the mass fraction of PAHs to range from 0.47 per cent to 7.32 per cent. Furthermore, we allow the exponent of power-law distribution to span a range of 1.5 to 2.5 in intervals of 0.5. While there is some evidence for a metallicity gradient (E. Sextl et al. 2024), this can be clouded by the metallicity-attenuation degeneracy (e.g. B. C. Whitmore et al. 2023), and thus we opt to use a standard metallicity of $Z = 0.02$ for consistency, as was done in J. A. Turner et al. (2021) and K. F. Henny et al. (2025). For the nebular emission model, we set the ionization parameter to $\log(U) = -2.0$, electron density (n_e) = 100, and allow the fraction of Lyman continuum photons escaping the galaxy ($f_{\rm esc}$) to reach all the way to 100 per cent, as done in K. F. Henny et al. (2025). We also assume a Chabrier Initial Mass Function (G. Chabrier 2003) with an upper mass limit of 100 $\mathrm{M}_\odot$, BC03 (G. Bruzual & S. Charlot 2003) simple stellar population (SSP) models, and also assume a dust attenuation-modified starburst model (modified from D. Calzetti et al. 2000's attenuation law).

These parameters were chosen after many model adjustments to the above parameters, including more expansive age grids (up to 13.7 Gyr) and $E(B-V)$ grids (up to 10 mag). However, these changes did not affect our statistical findings and resulted in overall much worse SED-fits, and thus we believe our final selection offers the best reasonable constraints for our sample. We have also tested the updated Charlot & Bruzual SSP models (A. Plat et al. 2019), however we found these SSP models not to be reliable for our specific use case (see Appendix C for further details).

3 RESULTS

3.1 Results of SED-fitting

As we have five different samples of objects based on their selection criteria, we can utilize SED-fitting to analyse whether the SED-fit properties of SF regions change based on the waveband with which they are identified. With CIGALE (M. Boquien et al. 2019), we use χ^2 minimization fitting of the photometry of each object from its *HST* & *JWST* images (*F275W*, *F336W*, *F438W*, *F555W*, *F814W*, *F200W*, *F300M*, *F335M*, *F360M*, *F770W*, *F1000W*, *F1130W*, *F2100W*) in order to estimate the mass-weighted, best-fitting stellar age (in Myr), $E(B-V)$ (in mag), and stellar mass (in $\mathrm{M}_\odot$) to examine these physical comparisons. We present here the statistics of our central population of SF regions, on which most of our analysis will occur, however we also examine the non-central *F2100W* sources for comparison and discuss them in more detail in Section 4.2.

We display the cumulative distribution functions of each of our subsample's SED ages in the top plot of Fig. 7. By determination of our SED fitting, the *HST*-selected sources are found to have the oldest modelled ages, with a median [25th percentile, 75th percentile] SED age of 9.3 Myr [4.9, 15.7]. The PAH-selected sources are the next oldest and have a median SED age of 7.2 Myr [4.7, 9.6]. The next youngest are the 10- and 21 μm-identified sources at medians of 4.9 Myr [3.1, 9.3] and 5.3 Myr [2.9, 7.6], respectively. The ALMA identified sources are modelled to be the youngest with a median SED age of 4.4 Myr [2.0, 9.3]. We also perform Kolmogorov–Smirnov (KS) tests to examine whether the distributions are significantly different, as measured by p-value. The distribution most likely to be drawn from a unique distribution is for the ages of ALMA sources, with p-values < 0.1 compared to all other distributions ($\sim 2\sigma$). The *HST* distribution has a p-value of ∼0.15 compared to the 10 and 21 μm distributions, indicating that the samples are drawn from unique distributions at a bit above the 1σ level. Placed between the *HST* and 10 and 21 μm distributions, the age distribution of PAH sources appears to be the least unique, with p-values of ∼0.3-0.4 ($\sim 1\sigma$) compared to those neighbouring distributions.

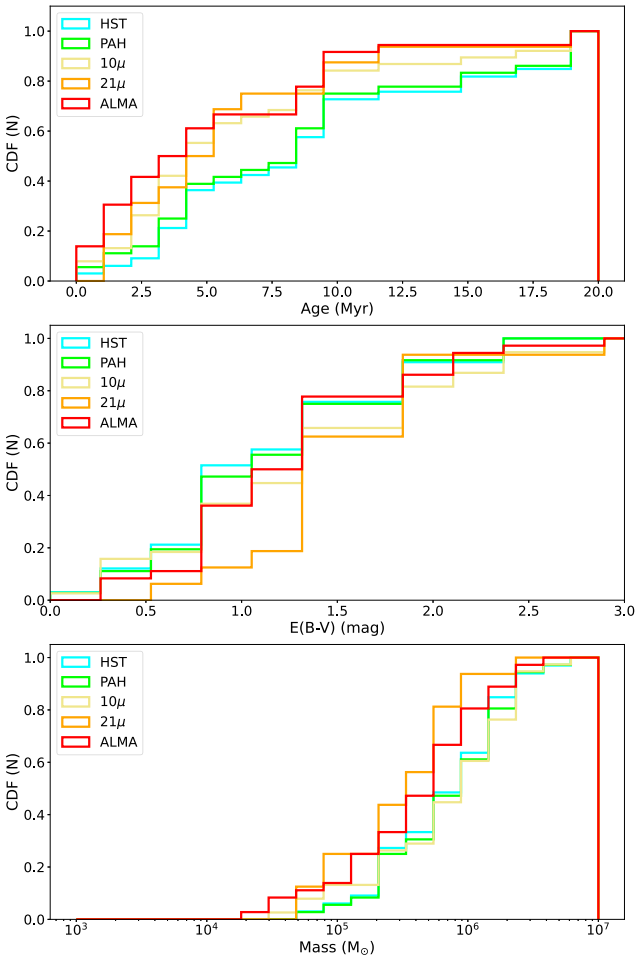

Figure 7. Cumulative distribution functions for the age (in Myr; top plot), reddening ($E(B-V)$, in mag; middle plot), and stellar mass (in $M_\odot$; bottom plot) of SF regions based on the catalogue from which they were selected. If a source is identified in multiple catalogues, they are included in each catalogue's distribution. Blue, green, yellow, orange, and red lines correspond to SF regions selected with *HST*, PAH, 10, 21 μm, and ALMA, respectively.

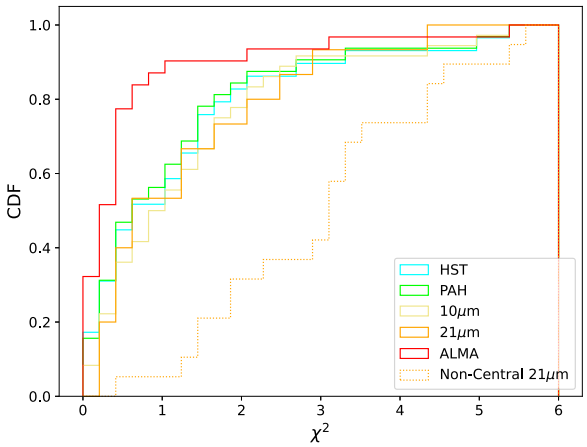

Figure 8. Cumulative distribution functions of reduced χ^2 metric from the SED-fitting of SF regions using CIGALE. Generally, we observe that the redder wavelength at which a source has been identified, the more likely that object will be underfit by the models. The ALMA sources, however, break this trend as they represent the most overfit sample of objects. Most of the non-central 21 μm sources reside outside *HST*'s field of view, contributing to their worse fits.

We note that the absolute ages we present are older than expected, as has also been seen in other works using CIGALE such as A. Pedrini et al. (2025), who found SED ages of over 6 Myr for strong Paα emitters, which should be much younger. There are currently limitations with CIGALE's energy balance principle in the context of SED fitting with *JWST*'s more diffuse emission (see K. F. Henny et al. (2025) for further details). However, the relative ages here and in the context of discussion in Section 4.1 align with prior results, and the focus of subsequent analysis will be primarily based on these relative results. Of the sources with matches in the catalogues of properties based on SED fitting of the photometry from the original *HST* images (D. A. Thilker et al. 2025), the majority of their ages from our fitting remain within ∼2 Myr of the original *HST*-based results, however it is important to reiterate here that, by using the 0.67 arcsec resolution, we are including the immediate surroundings in our photometry, which can result in slightly inflated ages (also discussed in Section 4.1). For a safe estimate, we consider the absolute ages presented in this work to be within a factor of two of their true ages. We believe that while this relative comparison is suitable for this work, the continued effort of improving SED modelling of *JWST's* more diffuse emission is important to understanding the absolute timescales at work in extremely young, embedded sources.

Along with having the oldest ages, the *HST*-selected sources generally have the smallest estimated $E(B-V)$ values, as expected for older sources. The cumulative distribution functions for each of our subsample's $E(B-V)$ values are shown in the middle panel of Fig. 7. Our *HST* sources have median $E(B-V)$ estimates of 0.88 mag [0.77, 1.41]. Interestingly, our ALMA sources have the next smallest $E(B-V)$ estimates at a median of 1.21 mag [0.97, 1.51]. This may be attributed to the fact that they have relatively weaker SED fits, with a median reduced χ^2 of 0.5 [0.2, 1.0] (Fig. 8). Many of these sources have weaker flux in the actual wavebands used for SED-fitting, making it harder to distinguish the signal from noise. The ALMA sources also have generally lower stellar mass estimates (distributions shown in the bottom panel of Fig. 7), which might be linked to their lower $E(B-V)$ estimates. As this catalogue is expected to mostly pick out sources in the early highly embedded phase (e.g. J. Sun et al. 2024), this could point to an underestimate of the actual $E(B-V)$ due to the limited actual detections across all filters available for fitting and potentially our imposed limit of $E(B-V)$. We find that the most overfit ALMA-selected sources ($\chi^2 < 0.2$; $N = 10$) all do not have detections in any of *HST*'s *B*, *V*, and *I* bands, and the overfitting of the model for these sources is associated with both lower $E(B-V)$ estimates (median of 0.99 mag) and higher age estimates (median of 7.3 Myr) than the rest of the ALMA sample (Table 2).

The PAH-, 10, and 21 μm-selected sources all have fairly similar distributions of $E(B-V)$, with median estimates of 1.43 mag [1.05, 1.93], 1.32 mag [0.88, 1.93], and 1.32 mag [1.32, 2.00], respectively. Here, mass again appears to be a correlated factor, as the PAH-selected sources we have identified in NGC 1365 are the most massive with a median of 16 [6.2, 24] (in 10^5 $M_\odot$), while the 10 μm-selected sources have a median of 9.7 [3.5, 22] (10^5 $M_\odot$) and the 21 μm-selected sources represent the least massive subsample with a median of 4.0 [2.0, 8.3] (10^5 $M_\odot$). Factoring in the differences in stellar mass between the samples, the SED-

Table 2. Statistical properties of NGC 1365's central star clusters as determined by our SED fitting, split up according to the catalogue with which they were identified. Median SED ages, $E(B-V)$s, masses, and goodness of fit (as measured by the reduced χ^2), along with the standard deviation and [25th, 75th] percentiles are provided for each sample.

SED Estimate	Age (Myr)	$E(B-V)$	Mass (10^5 $M_\odot$)	Reduced χ^2
HST	9.3 + /− 6.0 [4.9, 15.7]	0.88 + /− 0.54 [0.77, 1.41]	8.0 + /− 13 [3.0, 12]	1.2 + /− 4.1 [0.3, 2.7]
PAH	7.2 + /− 5.2 [4.7, 9.6]	1.43 + /− 0.57 [1.05, 1.93]	16 + /− 9.0 [6.2, 24]	0.8 + /− 0.7 [0.4, 1.5]
10 μm	4.9 + /− 5.3 [3.1, 9.3]	1.32 + /− 0.74 [0.88, 1.93]	9.7 + /− 13 [3.5, 22]	1.1 + /− 2.3 [0.6, 2.1]
21 μm	5.3 + /− 4.6 [2.9, 7.6]	1.32 + /− 0.55 [1.32, 2.00]	4.0 + /− 6.2 [2.0, 8.3]	1.0 + /− 1.7 [0.5, 2.2]
ALMA	4.4 + /− 4.7 [2.0, 9.3]	1.21 + /− 0.60 [0.97, 1.51]	5.6 + /− 8.8 [2.4,12]	0.5 + /− 5.0 [0.2, 1.0]

estimated $E(B-V)$ values of our sources other than the poorly-fit ALMA sources generally agree with our expectation that younger objects have larger $E(B-V)$ values, or conversely that the older objects have smaller $E(B-V)$ values.

Lastly, we also find agreement in the age trends for SF regions that are uniquely identified in one of the original source catalogues, as well as those which had matches across multiple catalogues. We have noted in Section 2 that there is some overlap between the original source catalogues from which we curated the overall sample for this study. There are 12 objects that are uniquely identified in B. C. Whitmore et al. (2023)'s *HST*- and PAH-based catalogue (34 per cent of that sample) and not in the 10, 21 μm, or ALMA catalogues, while the remaining 23 (66 per cent) from their sample are identified in at least one of those other catalogues. Similarly, there are nine sources unique to the 10 μm catalogue (24 per cent), eight sources unique to the central population of 21 μm-identified objects (50 per cent), and 14 sources unique to the ALMA catalogue (39 per cent). Table D1 displays the statistical SED ages, $E(B-V)$ values, and masses of these uniquely identified sources (similar to Table 2), where we find that the above statistical trends hold.

The same is also generally true for the SF regions that are identified in multiple source catalogues. As could be expected, these sources are brighter than their unique counterparts (by median ∼10–1000 per cent greater flux across their SEDs) and consequently more massive, however we also note some differences in their estimated ages. We find that sources unique to the *HST*- and PAH-based catalogue are, by median, ∼1–2 Myr older than those which had matches in other catalogues. Conversely, sources unique to the 10, 21 μm, and ALMA catalogues are ∼1–2 Myr younger than those which were identified in other catalogues, and we find this to be largely driven by sources that have also been identified in the *HST*- and PAH-based catalogue in particular. Although the trend here is weaker, the median SED ages of these not-uniquely identified SF regions still get progressively younger as you move from the catalogues of bluer to redder wavebands.

4 DISCUSSION

4.1 Age-distinguishing SED features

Until now, our analysis has mostly comprised of how the SED-fit properties of SF regions vary based on how they were selected, i.e. with *HST*, PAH, *F1000W*, *F2100W*, or ALMA. However, we can delve deeper into the specific features which help determine their ages in particular by examining the actual SEDs of these objects rather than only relying on their selection criteria.

Fig. 9 displays the median photometry across the wavebands used for the SED fitting for each group of sources according to the bands in which they were identified. Additionally, model SEDs of three star clusters have been added for reference, one of a 1 Myr cluster with high extinction [$E(B-V)=5$ mag], one slightly older (3 Myr), less-extincted cluster [$E(B-V)=1$ mag], and one older cluster (10 Myr) with low extinction [$E(B-V]=0.1$ mag), each having a mass of $\sim10^5$ $M_\odot$. Additionally, we provide all of the individual SEDs of our sample in Fig. D1 of Appendix D for reference.

One of the distinguishing features of the older, exposed SF regions is that the flux declines across the NIRCam bands (from 2 to 3.6 μm). As a test, we examine the near-infrared slopes of each of our sources in the upper plot of Fig. 10. In this plot, we use a simple average of the continuum sampled at 3 and 3.6 μm and compare it to the flux at 2 μm, where a value of 1 on the *y*-axis (indicated by a black, dashed line) indicates a flat near-infrared slope, and values greater than or less than one indicate positive or negative near-infrared slopes, respectively. If we simply divide the sample into sources with positive or negative near-infrared slopes, we find a clear difference in the best-fitting SED ages of the resultant samples: the sources with negative slopes are ∼64 per cent older than those with positive slopes by median age (7.2 Myr versus 4.4 Myr). KS tests also show the statistical significance of the difference between the SED ages of these two samples, and with these we find a *p*-value of ∼0.01, or a bit above 2σ.

We also observe that the SF regions identified at redder wavelengths (yellow, orange, and red points represent 10, 21 μm-, and ALMA-selected sources, respectively) tend to be the objects with positive slopes while the *HST*-selected sources tend to be those with negative slopes, which is sensible as the *HST*-selected sources are more likely to have cleared their natal gas while the objects identified at the redder wavelengths would still be surrounded by it. This is in agreement with K. F. Henny et al. (2025), where the near-infrared slope was one of the primary components used to help distinguish younger clusters from older ones, because young massive stars should be capable of heating their surrounding dust and thus elevate the emission in the near-infrared regime above the stellar continuum if dust is present. Since we do not see hot dust emission, as indicated by the negative infrared slope in these *HST*-selected objects, they are likely to have intermediate ages, and their positive optical slopes are thus due to a combination of redder stellar populations and some reddening. This is also in agreement with the statistical results from our SED-fitting (Section 3.1), which showed that they have intermediate ages.

Further quantifying this feature, we perform a linear least-squares regression between the SED age and the near-infrared slope of our sample of massive SF regions. We specifically fit the points of the sources with ages $\leq$ 10 Myr, where the true development is expected to occur, and the older points appear to level out. Although considerable scatter is observed, there appears to be a trend that shows age increases as the near-infrared slope

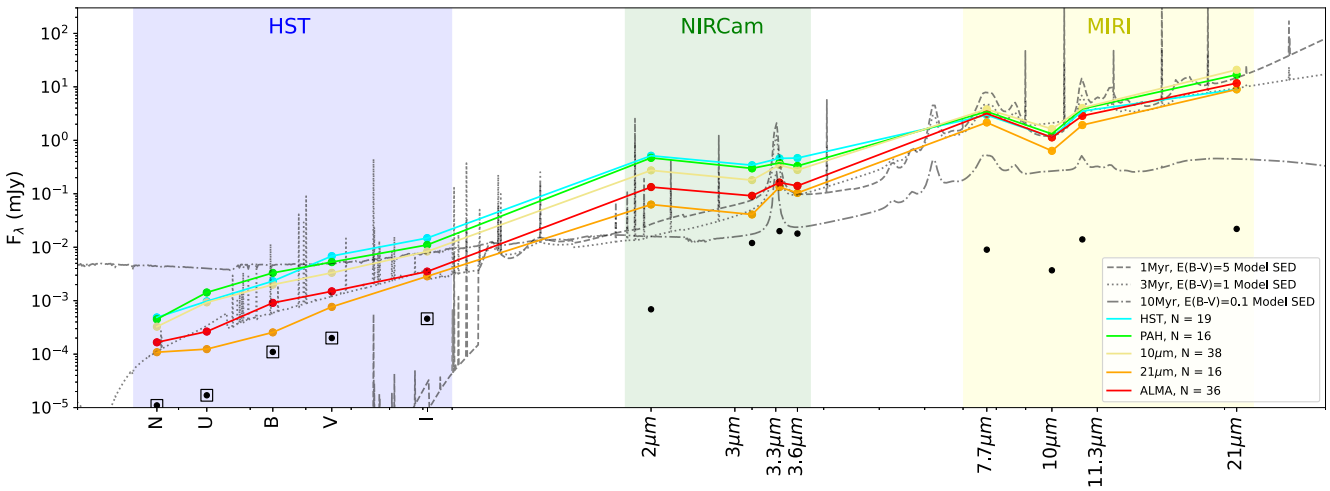

Figure 9. SEDs of SF regions in the central, starbursting region of NGC 1365, split up by the method by which they were identified. Flux density (in mJy) is plotted for each photometric waveband used for the SED-fitting with CIGALE. Here we show only the median SED for each of the five catalogues in our sample for comparison (HST-, PAH-, 10, 21 μm-, and ALMA-selected sources), which are constructed from the median flux densities in each waveband. Additionally, we include model SEDs from CIGALE of three clusters: a 1 Myr, $E(B-V) = 5$ mag cluster, a 3 Myr, $E(B-V) = 1$ mag cluster, and a 10 Myr, $E(B-V) = 0.1$ mag cluster for reference, each having a mass of $\sim 10^5$ $M_\odot$. Lastly, the black dots represent the smallest upper limit used for sources with non-detections in each band, and squared dots represent the bands in which 20–30 per cent of all sources used an upper limit value for its photometry (most others are below 10 per cent). All of the individual SEDs are presented for each subsample in separate plots in Fig. D1 of Appendix D.

decreases ($p = 1.6 \times 10^{-4}$, or $> 3\sigma$). Following the line of best fit, we find that the turnover in the near-infrared slope (from positive to negative slope) occurs around ∼6 Myr. This fitting is displayed in the top-right plot of Fig. 11, where we also include the corresponding Pearson coefficient and *p*-value. Since the clearing of gas and dust generally begins even earlier than this (within a few Myr; e.g. B. C. Whitmore et al. 2011; K. Hollyhead et al. 2015; S. Hannon et al. 2022), the true turnover is likely even earlier than this 6 Myr. However, because of our 0.67 arcsec resolution, we are capturing emission from the gas and dust which may have already been cleared from a cluster itself but remains in the immediate surroundings in the first several Myr (e.g. B. C. Whitmore et al. 2014; J. Kim et al. 2021). Thus, this metric stands as a reasonable estimate for younger, massive SF regions in general.

Another feature of older objects is weaker dust emission, which we have observed in our MIRI wavebands, as the youngest objects should be the most capable of heating their surrounding dust. We examine this feature in the central plot of Fig. 10, which displays the stellar continuum of our massive SF regions sampled at 2 μm versus the relative strength of their emission from larger dust grains at 21 μm. Here we find that the sources with the strongest ratio of 21 to 2 μm are the youngest according to their SED-fit ages. SF regions which have a relative flux of $F_{21\mu m}/F_{2\mu m} > 300$ have a median SED age of 3 Myr, and the sources have older SED-fit ages as that ratio declines: those with $40 < F_{21\mu m}/F_{2\mu m} < 300$ have a median SED age of 5 Myr, and those with $F_{21\mu m}/F_{2\mu m} < 40$ have a median SED age of 9 Myr. Again, the points here are colour-coded according to their identification catalogue, and we find that the SF regions identified in the redder wavelengths tend to have the largest $F_{21\mu m}/F_{2\mu m}$ ratios while those identified in the bluer wavebands have the smallest such ratios, as expected (e.g. the *HST*-selected sources have the highest median F200W flux density, but the lowest median F2100W flux density). With *p*-values all less than 0.02, KS tests show that the mean SED ages in each of these three bins are fairly unique with a significance greater than 2σ. The bins of the smallest and largest $F_{21\mu m}/F_{2\mu m}$, however, show considerably more significant differences, with a *p*-value of 5.2×10^{-7}. The smallest and middle $F_{21\mu m}/F_{2\mu m}$ bins are similarly unique with a *p*-value of 4.6×10^{-5}. This metric is plotted versus SED age in the top-left plot of Fig. 11, where a least-squares fit also shows that this correlation is strong ($>3\sigma$).

While we observe more variance in the median 2 μm flux between the catalogues (Fig. 9), we find the predictive power for ages to be much stronger with the $F_{21\mu m}/F_{2\mu m}$ ratio than with $F_{2\mu m}$ alone. The variation in individual SEDs are shown in Fig. D1 of Appendix D, where we observe that the $F_{21\mu m}/F_{2\mu m}$ ratio is similar in size to the $F_{2\mu m}/B$ ratio. This is because the reservoir of gas and dust is less eroded in younger SF regions than in older, more exposed regions, and thus the relative dust emission is stronger in the younger regions. Statistically, we observe that the relation between $F_{2\mu m}$ and age produces a much weaker Pearson coefficient (0.14) compared to the $F_{21\mu m}/F_{2\mu m}$ versus age relationship ($p = 6.1 \times 10^{-4}$), and we find that this difference is largely due to the $F_{21\mu m}/F_{2\mu m}$ ratio being able to distinguish the youngest SF regions (<3 Myr), whereas $F_{2\mu m}$ alone cannot do so for our sample.

One last prominent feature that differentiates the younger and older SF regions and is identifiable in Fig. 9 is that of PAH emission bands. Amongst our data we have three wavebands which detect PAHs: F335M, which is the primary PAH-tracing band, as well as F770W and F1130W, which trace ionized PAH molecules and larger, neutral PAH molecules, respectively (e.g. A. Maragkoudakis, E. Peeters & A. Ricca 2020). We also have an accompanying continuum sample near the 3.3 μm feature with F300M, which largely traces starlight. As displayed in Fig. 9, there are clear peaks in emission at each of these wavelengths for the two younger cluster models, while those peaks are noticeably absent for the 10 Myr cluster. The strongest of these peaks occurs at the main PAH-tracing band at 3.3 μm. We plot the distribution of our SF regions' fluxes at 3.3 μm relative to the nearby

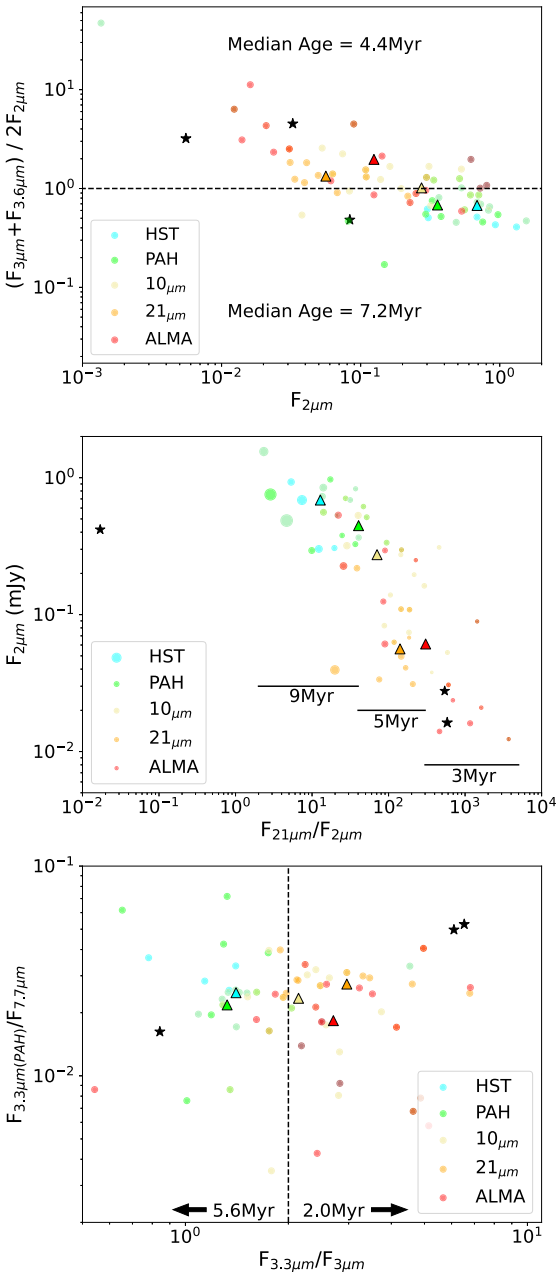

Figure 10. Comparisons of massive SF regions in the centre of NGC 1365 based on apparent distinguishing features of their SEDs. Each plot displays sources with colours corresponding to the catalogue from which they were selected (*HST* = cyan points, PAH = green points, 10 μm = yellow points, 21 μm = orange points, ALMA = red points), and triangles indicate the median values for each catalogue. On the top, we examine the strength of dust emission relative to the stellar continuum with the ratio of $F_{21\mu m}/F_{2\mu m}$. The middle plot displays the near-infrared slope, which we have determined by using the average of the two continuum samples with F300M and F360M relative to the stellar continuum with F200W. In the bottom plot we show the ratio of $F_{3.3\mu m}/F_{3\mu m}$ as a reasonable estimate of the degree of PAH emission on the *x*-axis, and the PAH bandpass ratio $F335M_{PAH}/F770W$ (see Section 4.1) on the *y*-axis. This last feature is the only one of the four which does not show an apparent correlation, and is also not apparent in an equivalent plot with $F335M_{PAH}/F1130W$. Each plot includes the positions of the model clusters shown in Fig. 9, indicated by black stars, as well as the median SED ages of all of the SF regions in the indicated regions.

stellar continuum at 3 μm on the *x*-axis of the lower plot in Fig. 10. This assumes that F300M is relatively uncontaminated, and therefore this ratio gives a reasonable estimate of the degree of PAH emission. With this metric, we find another noticeable difference in the ages of the sources along this axis, where those with $F_{3.3\mu m}/F_{3\mu m} > 2$ have a median age of 2.0 Myr compared to 5.6 Myr for those which have $F_{3.3\mu m}/F_{3\mu m} < 2$. The least-squares fit shown in the bottom-left plot of Fig. 11 supports this, however it is weaker (*p*-value of 0.049) than the previous metrics, which is potentially due to some contamination of PAH emission in the *F300M* filter.

K. M. Sandstrom et al. (2023) devised another method to remove the stellar continuum from the 3.3 μm feature and named the resultant PAH emission there $F335M_{PAH}$, defined as the difference between the flux at F335M and an estimation of the continuum at 3.3 μm as $A \times$F300M $+ B \times$ F360M, where they adopt coefficients of $A_{Lai} = 0.35$ and $B_{Lai} = 0.65$ (T. S. Y. Lai et al. 2020). D. A. Dale et al. (2023) were able to show a correlation between the estimated stellar age of star clusters and PAH bandpass flux ratios ($F335M_{PAH}$ divided by each of F770W & F1130W), which are expected to trace the average size and ionization level of the dust grains (A. Maragkoudakis et al. 2020, 2022; B. T. Draine et al. 2021; D. Rigopoulou et al. 2021). They found that within their catalogue of star clusters and stellar associations in PHANGS galaxies, larger such ratios corresponded to younger objects. We have plotted the PAH passband ratio of $F335M_{PAH}/F770W$ on the *y*-axis of the bottom plot of Fig. 10, however we do not observe a clear correlation with SED age in our data as we have for the prior features (nor with $F335M_{PAH}/F1130W$). The least-squares fit (shown in the bottom-right plot of Fig. 11) actually shows a very slight correlation contrary to D. A. Dale et al. (2023), though it is by far the weakest (*p*-value of 0.263) of all the metrics. While this may be related to the degraded resolution of our images and/or the presence of additional contributions arising from hot dust or continuum emission in the PAH-tracing MIRI bands, this relatively flat trend agrees with the results of A. Pedrini et al. (2024), who found that the ratio of PAH emission remains constant over a source's first 10 Myr, regardless of its morphology (compact, extended, and open PAH radial profiles).

Thus we identify three features of our SEDs which appear to correlate with the age of SF regions: the slope of the near-infrared spectrum $[(F_{3\mu m} + F_{3.6\mu m})/(2F_{2\mu m})]$, the relative strength of emission from larger dust grains ($F_{21\mu m}/F_{2\mu m}$), and the relative strength of PAH emission ($F_{3.3\mu m}/F_{3\mu m}$). Older populations of stars lack the capability of heating dust in the near-infrared (NIR) and mid-infrared (MIR) wavebands, and thus positive NIR slopes as well as stronger relative emission in the PAH-tracing 3.3 μm and larger dust-tracing 21 μm wavebands are all indicators of younger (<10Myr) stellar populations. Again we note that these features are robust to not just individual star clusters, but also the inclusion of emission from surrounding gas and dust by virtue of the 0.67 arcsec working resolution in this study.

4.2 Non-central 21 μm-selected sources

In Section 2, we noted that 23 of our 39 sources selected with *F2100W* were located outside of the central region of NGC 1365. While we have focused our analysis thus far on the centre, these non-central sources allow us to examine how they differ from the central 21 μm sources. Further, 16 of these non-central sources are located outside of the field of view of the *HST* broad-band images, and thus allow us to see how the SED fitting performs for

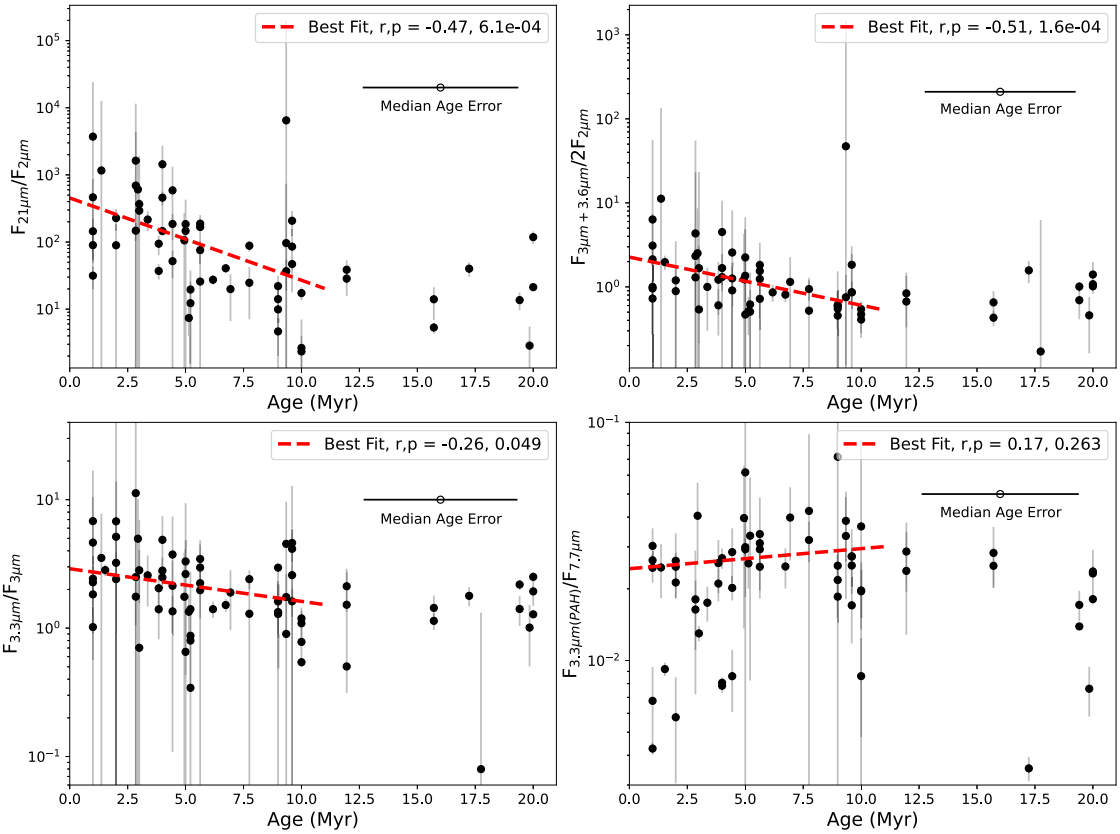

Figure 11. Comparisons between estimated SED age and various features from the SEDs for all of the SF regions in our sample: dust emission sampled from $F_{21\mu m}/F_{2\mu m}$ (top left), near-infrared slope sampled from the ratio of the average of F300M and F360M to the stellar continuum at F200W (top-right, estimated strength of PAH emission measured as the ratio of $F_{3.3\mu m}/F_{3\mu m}$ (bottom-left), and the PAH passband ratio (F335M$_{PAH}$/F770W; bottom-right). Vertical error bars representing combined photometric errors are provided for each point, and the median Bayesian error in the age of sources is shown in the upper-right corner of each plot separately for better clarity. We note that the F335M$_{PAH}$/F1130W passband ratio is qualitatively and quantitatively similar. Additionally, in each plot we include a least-squares fit of the sources with ages $\leq$ 10 Myr (where the true development is expected to occur), as well as the corresponding Pearson coefficient (r) and p-values.

these potentially dusty sources while lacking *HST* photometry. As discussed below, we also refit the central SF regions without the *HST* bands and find consistent results across their median ages, $E(B-V)$ values, and masses.

By splitting the 21 μm sample into those which are central (N = 16) and those which are non-central (N = 23), we find some notable differences from their best-fit SED properties. The most prominent difference is that the non-central sources, both those with and without *HST* photometry available, generally have considerably lower SED masses (combined median [25th percentile, 75th percentile] of 0.43 [0.21, 0.68], in 10^5 M$_\odot$), despite the flux criteria we used for selection (see Section 2). This is about one full magnitude lower than the central 21 μm sample. Along with the lower masses, we also find that these sources have older SED ages and lower SED $E(B-V)$ values. Non-central sources with *HST* available have a median SED age of 9.5 Myr [6.7, 13.4] and a median $E(B-V)$ of 0.68 mag [0.34, 1.02]. Non-central SF regions without *HST* have a median SED age of 7.7 Myr [5.5, 13.4] and a median $E(B-V)$ of 0.68 mag [0.34, 1.02]. Performing KS tests on the distributions shows that while the mean SED ages are not dissimilar to the central sample of 21 μm sources (p-values of ∼0.15), the differences between their $E(B-V)$ values are more, but not entirely, significant (p-values of ∼0.01, or $>2\sigma$). As discussed in Section 3.1, the lower-estimated $E(B-V)$ values could at least in part be attributed to the lower masses of the non-central sample (see Section 3.1). Estimated $E(B-V)$ values and stellar masses of the central versus non-central 21 μm samples are displayed in Fig. 12, where a scattered correlation between mass and $E(B-V)$ is evident, along with the lower $E(B-V)$ values and masses of the non-central sample. We note that the singular, massive (∼ 10^7 M$_\odot$) non-central point in this plot is outside of NIRCam's field of view, thus only having MIRI photometry, and may in fact be a background galaxy.

The other most notable difference between the central and non-central 21 μm samples is their goodness of fits. The combined median reduced χ^2 [25th percentile, 75th percentile] of the 23 non-central sources is 3.3 [1.9, 4.7]. This represents considerably worse SED fitting compared to the central sample, whose median χ^2 is 1.0 [0.5, 2.2]. Additionally, while we fit the non-central sources without *HST* photometry without those filters in CIGALE, we also fit our central 21 μm sample without the *HST* photometry for comparison. We find that by removing the *HST* data, many SF regions have worse reduced χ^2 values (medians of 0.79 versus 1.0 for the *HST*-included SED-fits) and have slightly different best ages and $E(B-V)$ values, however the median SED age and $E(B-V)$ of the central 21 μm sample actually remains unchanged, which may be expected as these sources are likely dusty and have little flux in the *HST* wavebands to begin with.

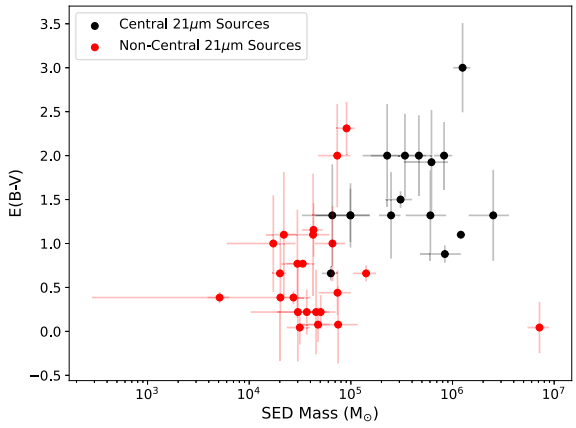

Figure 12. $E(B-V)$ versus stellar mass of 21 μm-identified sources, as determined by our SED fitting (Section 2.5). Bayesian errors in the SED-fit masses and $E(B-V)$s are also provided for each point. SF regions which are located in the central region of NGC1365 are represented by black points, while the non-central sources are represented by red points. While the non-central sources have much lower SED-estimated $E(B-V)$ and mass compared to the central sources, they are also out of the field of view of our *HST* images, and thus lack its photometry which is crucial for accurate SED fitting with CIGALE.

The median SED age of central 21 μm SF regions without the use of *HST* photometry is 5.3 Myr [4.8,7.5], and the median SED $E(B-V)$ is 1.35 mag [0.69, 2.13], both of which are in line with the *HST*-included SED fits presented in Table 2. By comparing these results to those which include the *HST* photometry, we find that the main difference in the reduced χ^2 appears to stem from how the model interprets the younger and older populations within a SF region: the median mass attributed to the young stars is five times greater in the sample which includes *HST*, and along with that the mass of the older stars is ∼50 per cent greater in the sample without *HST*. All other parameters remain within ∼10 per cent of each other. For our purposes, while the inclusion of *HST* photometry may not affect the population-level statistical properties of our 21 μm-selected sources, it does considerably improve how well the SF regions' SEDs are fit with CIGALE, and should be used to ensure quality fits.

5 SUMMARY

We investigate the properties of the population of massive star-forming regions in the centre of NGC 1365 by combining five source catalogues, each selecting objects at different wavelengths, spanning from optical to millimeter emission. This includes *HST*- and PAH-selected sources (B. C. Whitmore et al. 2023; D. Maschmann et al. 2024), 10 μm-selected sources (E. Schinnerer et al. 2023), 21 μm-selected sources (H. Hassani et al. 2023), and ALMA-selected sources (this work). Altogether, the combined catalogue is comprised of 85 unique, centrally located star-forming regions.

Prior to photometry, we first address the issue of saturation in our *JWST*/MIRI images. While all four of our MIRI images (*F770W*, *F1000W*, *F1130W*, and *F2100W*) exhibit some degree of saturation effects, *F2100W* represents the image which is most affected, as we observe 32 of our 85 sources (38 per cent) are either completely saturated or at least affected by it. To ameliorate these effects, we experiment by modifying both the RSCD and first frame correction steps in the pipeline described in T. G. Williams et al. (2024). We find more valid resultant images by changing only the RSCD step, which allows us to include additional frames and thus data for the saturation-affected areas, and the use of these images in place of the standard pipeline images helps us recover reasonable data for 23 of the 32 affected sources in *F2100W*.

After correcting images for saturation effects, we convolve each of the *HST*, *JWST*/NIRCam, *JWST*/MIRI, and ALMA images to match the resolution of our lowest-resolution image (*F2100W*; 0.67 arcsec), and perform photometry in each of our *HST* and *JWST* wavebands for SED-fitting with CIGALE (M. Boquien et al. 2019). With this convolution, we are not necessarily looking at indiviudal clusters, but also the emission in their immediate vicinity, hence our use of 'star-forming regions' (SF regions in this work) rather than specifically clusters. This fitting produces best-fitting SED ages, $E(B-V)$ values, and masses for our sample of objects, and allows us to compare their properties according to the waveband in which they were selected. Generally, we find that as the selection band increases in wavelength (i.e. from *HST* to ALMA), the median SED age of those SF regions decreases. The median SED age of the SF regions selected with *HST*, PAH, *F1000W*, *F2100W*, and ALMA are 9.3, 7.2, 4.9, 5.3, and 4.4 Myr, respectively. In the same order, we find median $E(B-V)$ values of 0.88, 1.43, 1.32, 1.32, and 1.21. However, these values are likely affected by the relative mass of each sample, where the more massive SF regions tend to have higher $E(B-V)$ values. With this in mind, our statistics follow that redder wavebands are detecting younger, more reddened sources.

We also examine the actual SEDs of the SF regions in order to determine features within the SEDs which inform the models of their age, regardless of the waveband from which they are selected. Since we use a working resolution of 0.67 arcsec, these characteristics are robust to the inclusion of the immediately surrounding emission of clusters. We find correlations with three such features: (1) The near-infrared slope (determined by an average of the F300M & F360M flux relative to the stellar continuum sampled at F200W), where we find that positive and negative slopes are indicative of younger (median SED age of 4.4 Myr) and older (median SED age of 7.2 Myr) SF regions, respectively. We find that the SEDs of SF regions change from a positive to negative NIR slope statistically around 6 Myr, in line with previous studies (e.g B. C. Whitmore et al. 2014; J. Kim et al. 2021). (2) The dust emission relative to the stellar continuum (determined by $F_{21\mu m}/F_{2\mu m}$) shows a progression of ages as the ratio of dust emission decreases (3 Myr for SF regions with $F_{21\mu m}/F_{2\mu m}) > 300$, 5 Myr for sources with $40 < F_{21\mu m}/F_{2\mu m}) < 300$, and 9 Myr for sources with $F_{21\mu m}/F_{2\mu m}) < 40$). (3) Stronger PAH emission estimated from $F_{3.3\mu m}/F_{3\mu m}$ indicates younger ages. We find that SF regions with $F_{3.3\mu m}/F_{3\mu m}$ greater than and less than 2 have median SED ages of 2.0 and 5.6 Myr, respectively.

Lastly, in addition to our centrally located sample of SF regions, we also identify 23 SF regions, detected with *F2100W*, that are found outside the central region of the galaxy, and we compare these sources to our central *F2100W*-selected sample. While we find that the median ages and $E(B-V)$ values of the non-central sample are in line with the properties of the central SF regions, we observe that they are considerably more poorly fit with CIGALE. This is likely due to the fact that 16 of the 23 (∼70 per cent) reside outside of *HST*'s field of view and thus completely lack *HST* photometry which is critical for accurate modelling of stellar

sources. In order to test the robustness of our central sample's statistics which we have presented, we additionally use CIGALE to fit the central *F2100W* sample without its *HST* photometry, whereupon we find that the removal of these wavebands degrades the quality of the fits; however, it does not affect the statistical properties of the sample.

ACKNOWLEDGEMENTS

This work is based on observations made with the NASA/ESA/CSA *James Webb Space Telescope* (programme #2107) and the NASA/ESA *Hubble Space Telescope* (programme #15654 & #17126). The data were obtained from the Mikulski Archive for Space Telescopes at the Space Telescope Science Institute, which is operated by the Association of Universities for Research in Astronomy, Inc., under NASA contract NAS 5–03127 for *JWST* and 5–26555 for *HST*. SH acknowledges funding from the DLR (German Aerospace Agency) via grant 50 OR 2212. MB gratefully acknowledges support from the ANID BASAL project FB210003. This work was supported by the French government through the France 2030 investment plan managed by the National Research Agency (ANR), as part of the Initiative of Excellence of Université Côte d'Azur under reference number ANR-15-IDEX-01. RSK acknowledges financial support from the European Research Council via the ERC Synergy Grant 'ECOGAL' (project ID 855130), from the German Excellence Strategy via the Heidelberg Cluster of Excellence (EXC 2181–390900948) 'STRUCTURES', and from the German Ministry for Economic Affairs and Climate Action in project 'MAINN' (funding ID 50OO2206). RSK is grateful for computing resources provided by the Ministry of Science, Research and the Arts (MWK) of the State of Baden – Württemberg through bwHPC and the German Science Foundation (DFG) through grants INST 35/1134-1 FUGG and 35/1597-1 FUGG, and also for data storage at SDS@hd funded through grants INST 35/1314-1 FUGG and INST 35/1503-1 FUGG. RSK also thanks the Harvard – Smithsonian Center for Astrophysics and the Radcliffe Institute for Advanced Studies for their hospitality during his sabbatical, and the 2024/25 Class of Radcliffe Fellows for highly interesting and stimulating discussions. DL acknowledges the support from the Strategic Priority Research Programme of the Chinese Academy of Sciences, grant no. XDB0800401. KK gratefully acknowledges funding from the Deutsche Forschungsgemeinschaft (DFG, German Research Foundation) in the form of an Emmy Noether Research Group (grant number KR4598/2-1, PI Kreckel) and the European Research Council's starting grant ERC StG-101077573 ('ISM-METALS'). KG was supported by the Australian Research Council through the Discovery Early Career Researcher Award (DECRA) Fellowship (project number DE220100766) funded by the Australian Government. KG was supported by the Australian Research Council Centre of Excellence for All Sky Astrophysics in 3 Dimensions (ASTRO 3D), through project number CE170100013. AW acknowledges UNAM's DGAPA for the support in carrying out her sabbatical stay at UCSD, USA, through programme PASPA.

DATA AVAILABILITY

The broad-band images used in this study are from the PHANGS collaboration (A. K. Leroy et al. 2021; E. Emsellem et al. 2022; J. C. Lee et al. 2022, 2023; https://phangs.stsci.edu), and are publicly available via MAST (https://mast.stsci.edu) and the ALMA Science Archive (https://almascience.eso.org/aq/). A list of the SF regions presented in this paper, including IDs, RAs, Decs, and photometry, is included as a Supplementary File with this paper.

REFERENCES

Adamo A. et al., 2020, MNRAS, 499, 3267
Anand G. S. et al., 2021a, AJ, 162, 80
Anand G. S. et al., 2021b, MNRAS, 501, 3621
Aniano G., Draine B. T., Gordon K. D., Sandstrom K., 2011, PASP, 123, 1218
Barth A. J., Ho L. C., Filippenko A. V., Sargent W. L., 1995, AJ, 110, 1009
Belfiore F. et al., 2023, A& A, 678, A129
Boquien M., Burgarella D., Roehlly Y., Buat V., Ciesla L., Corre D., Inoue A. K., Salas H., 2019, A&A, 622, A103
Bressan A., Marigo P., Girardi L., Salasnich B., Dal Cero C., Rubele S., Nanni A., 2012, MNRAS, 427, 127
Bruzual G., Charlot S., 2003, MNRAS, 344, 1000
Calzetti D., Armus L., Bohlin R. C., Kinney A. L., Koornneef J., Storchi-Bergmann T., 2000, ApJ, 533, 682
Calzetti D. et al., 2007, ApJ, 666, 870
Chabrier G., 2003, PASP, 115, 763
Chastenet J. et al., 2019, ApJ, 876, 62
Chen Y., Bressan A., Girardi L., Marigo P., Kong X., Lanza A., 2015, MNRAS, 452, 1068
Dale D. A. et al., 2023, ApJ, 944, L23
Deshmukh S. et al., 2024, ApJ, 974, L24
Draine B. T., 2003, ARA&A, 41, 241
Draine B. T., Li A., 2007, ApJ, 657, 810
Draine B. T. et al., 2014, ApJ, 780, 172
Draine B. T., Li A., Hensley B. S., Hunt L. K., Sandstrom K., Smith J. D. T., 2021, ApJ, 917, 3
Emsellem E. et al., 2022, A&A, 659, A191
Galliano F., Galametz M., Jones A. P., 2018, ARA&A, 56, 673
Grasha K. et al., 2018, MNRAS, 481, 1016
Grasha K. et al., 2019, MNRAS, 483, 4707
Hannon S. et al., 2019, MNRAS, 490, 4648
Hannon S. et al., 2022, MNRAS, 512, 1294
Harris W. E., 2003, A Decade of Hubble Space Telescope Science, Space Telescope Science Institute Symposium Series. Cambridge Univ. Press, Cambridge
Hassani H. et al., 2023, ApJ, 944, L21
Hassani H. et al., 2024, ApJS, 271, 2
Hassani H. et al., 2025, preprint (arXiv:2509.16459)
Henny K. F. et al., 2025, ApJ, 991, 76
Hollyhead K., Bastian N., Adamo A., Silva-Villa E., Dale J., Ryon J. E., Gazak Z., 2015, MNRAS, 449, 1106
Holtzman J. A. et al., 1992, AJ, 103, 691
Johnson K. E., Brogan C. L., Indebetouw R., Testi L., Wilner D. J., Reines A. E., Chen C. H. R., Vanzi L., 2018, ApJ, 853, 125
Kennicutt R. C., Evans N. J., 2012, ARA&A, 50, 531
Kim J. et al., 2021, MNRAS, 504, 487
Knutas A. et al., 2025, ApJ, 993, 13
Lada C. J., Lada E. A., 2003, ARA&A, 41, 57
Lai T. S. Y., Smith J. D. T., Baba S., Spoon H. W. W., Imanishi M., 2020, ApJ, 905, 55
Lee J. C. et al., 2022, ApJS, 258, 10
Lee J. C. et al., 2023, ApJ, 944, L17
Leroy A. K. et al., 2021, ApJS, 257, 43
Levy R. C. et al., 2022, ApJ, 935, 19
Li A., 2020, Nat. Astron., 4, 339
Linden S. T. et al., 2021, ApJ, 923, 278
Linden S. T. et al., 2024, ApJ, 974, L27
Liu D. et al., 2023, ApJ, 944, L19
Maragkoudakis A., Peeters E., Ricca A., 2020, MNRAS, 494, 642

Maragkoudakis A., Boersma C., Temi P., Bregman J. D., Allamandola L. J., 2022, ApJ, 931, 38
Marigo P., Bressan A., Nanni A., Girardi L., Pumo M. L., 2013, MNRAS, 434, 488
Maschmann D. et al., 2024, ApJS, 273, 14
Mathis J. S., Mezger P. G., Panagia N., 1983, A&A, 128, 212
Matthews A. M., Johnson K. E., Whitmore B. C., Brogan C. L., Leroy A. K., Indebetouw R., 2018, ApJ, 862, 147
McQuaid T. et al., 2024, ApJ, 967, 102
Messa M. et al., 2021, ApJ, 909, 121
Mohan N., Rafferty D., 2015, Astrophysics Source Code Library, record (ascl:1502.007)
Morganti R., Tsvetanov Z. I., Gallimore J., Allen M. G., 1999, A&AS, 137, 457
O'Connell R. W., Gallagher John S. I., Hunter D. A., 1994, ApJ, 433, 65
Pedrini A. et al., 2024, Ap,J, 971, 32
Pedrini A. et al., 2025, ApJ, 992, 96
Perrin M. D., Sivaramakrishnan A., Lajoie C.-P., Elliott E., Pueyo L., Ravindranath S., Albert L., 2014, in Oschmann J. M. J., Clampin M., Fazio G. G., MacEwen H. A., eds, Proc. SPIE Conf. Ser., Vol. 9143, Space Telescopes and Instrumentation 2014: Optical, Infrared, and Millimeter Wave. SPIE, Bellingham, p. 91433X
Plat A., Charlot S., Bruzual G., Feltre A., Vidal-García A., Morisset C., Chevallard J., Todt H., 2019, MNRAS, 490, 978
Portegies Zwart S. F., McMillan S. L. W., Gieles M., 2010, ARA&A, 48, 431
Rigopoulou D. et al., 2021, MNRAS, 504, 5287
Robitaille T., Rice T., Beaumont C., Ginsburg A., MacDonald B., Rosolowsky E., 2019, Astrophysics Source Code Library, record (ascl:1907.016)
Rodríguez M. J. et al., 2023, ApJ, 944, L26
Sandqvist A., Jorsater S., Lindblad P. O., 1982, A&A, 110, 336
Sandqvist A., Joersaeter S., Lindblad P. O., 1995, A&A, 295, 585
Sandstrom K. M. et al., 2023, ApJ, 944, L7
Schinnerer E., Leroy A. K., 2024, ARA&A, 62, 369
Schinnerer E. et al., 2023, ApJ, 944, L15
Sextl E. et al., 2024, ApJ, 960, 83
Smith J. D. T. et al., 2007, ApJ, 656, 770
Sun J. et al., 2024, ApJ, 967, 133
Thilker D. A. et al., 2025, ApJS, 280, 1
Tielens A. G. G. M., 2008, ARA&A, 46, 289
Turner J. A. et al., 2021, MNRAS, 502, 1366
de Vaucouleurs G., de Vaucouleurs A., Corwin Herold G. J., Buta R. J., Paturel G., Fouque P., 1991, Third Reference Catalogue of Bright Galaxies. Springer, New York, NY
Whitmore B. C., Schweizer F., Leitherer C., Borne K., Robert C., 1993, AJ, 106, 1354
Whitmore B. C. et al., 2011, ApJ, 729, 78
Whitmore B. C. et al., 2014, ApJ, 795, 156
Whitmore B. C. et al., 2021, MNRAS, 506, 5294
Whitmore B. C. et al., 2023, ApJ, 944, L14
Williams T. G. et al., 2024, ApJS, 273, 13

SUPPORTING INFORMATION

Supplementary data are available at *MNRAS* online.

Hannon_2025_Sample.tab

Please note: Oxford University Press is not responsible for the content or functionality of any supporting materials supplied by the authors. Any queries (other than missing material) should be directed to the corresponding author for the article.

APPENDIX A: DATA USED IN THE ANALYSIS

Orientation of the field of view covered by the datasets used in the analysis is presented in Fig. A1. The input images at a matched resolution of 0.67 arcsec are show in Fig. A2.

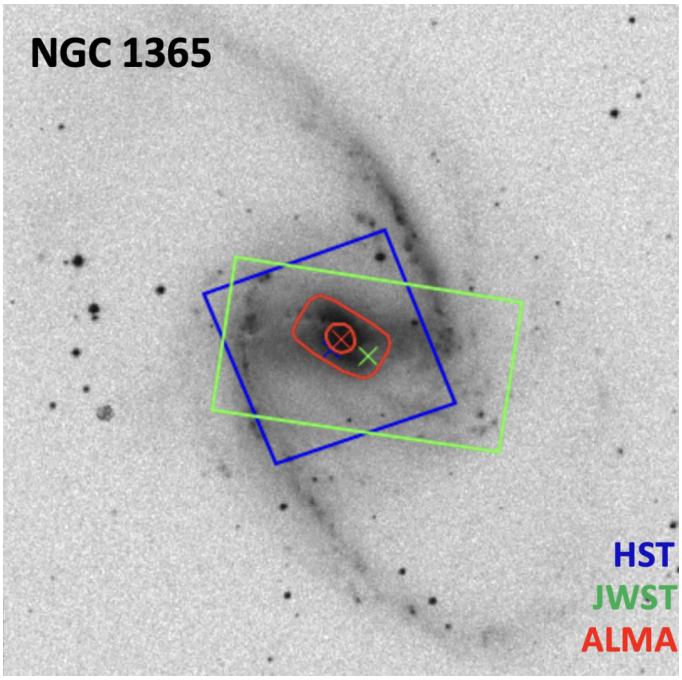

Figure A1. Footprints for each of the data sets used in this study overlaid on a 10 arcmin × 10 arcmin digitized sky survey image of NGC 1365. The field of view for our *HST* data is outlined in blue, *JWST* in green, and ALMA in red – the outer red border represents the 1.3 mm image, while the innermost is the 0.87 mm image.

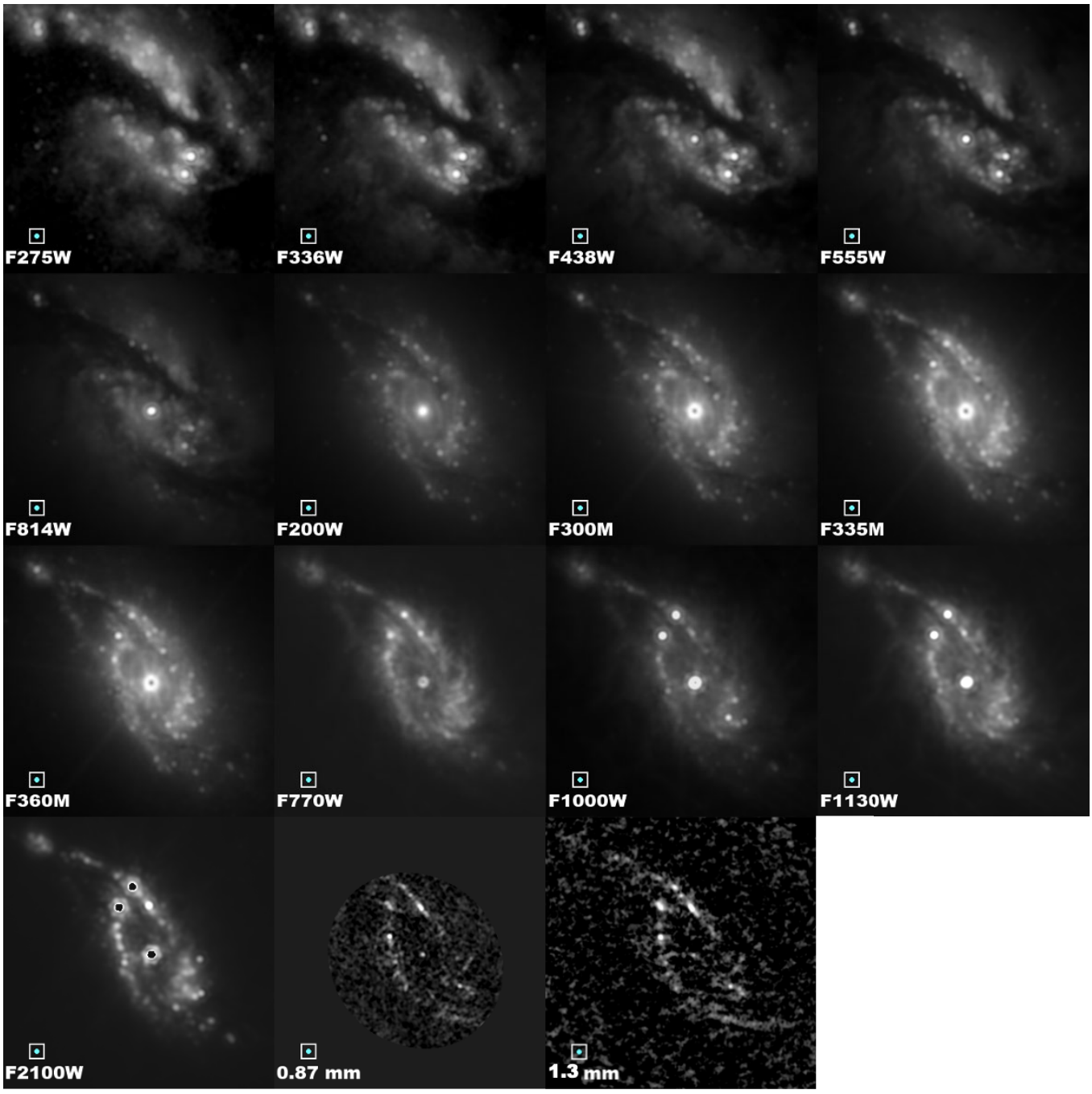

Figure A2. Complete sample of greyscale images for the central region of NGC 1365. The images are ∼4 kpc wide, observed with *HST*, *JWST*, and ALMA. Each of the images has been convolved to match the resolution of the MIRI *F2100W* filter, which has the lowest spatial resolution (FWHM of 0.67 arcmin). The filter name is labelled in the lower left of each image, along with a cyan dot above the filter to show the PSF of the *F2100W* image.

APPENDIX B: FURTHER TEST ON MIRI SATURATION CORRECTION

While our correction methods seem to have recovered a significant fraction of saturated sources, it is important to check the validity of our modified images, which we do by comparing them to the original pipeline images described in T. G. Williams et al. (2024). Figs B1 and B2 highlight the differences between our corrected images versus the original pipeline images for *F2100W* from a statistical point of view. Fig. B1 shows ratio maps of the corrected/original images for two correction methods: On the left, we show the differences when we apply changes to both the first frame step and RSCD step, and on the right are the differences when we only change the RSCD step. It is evident

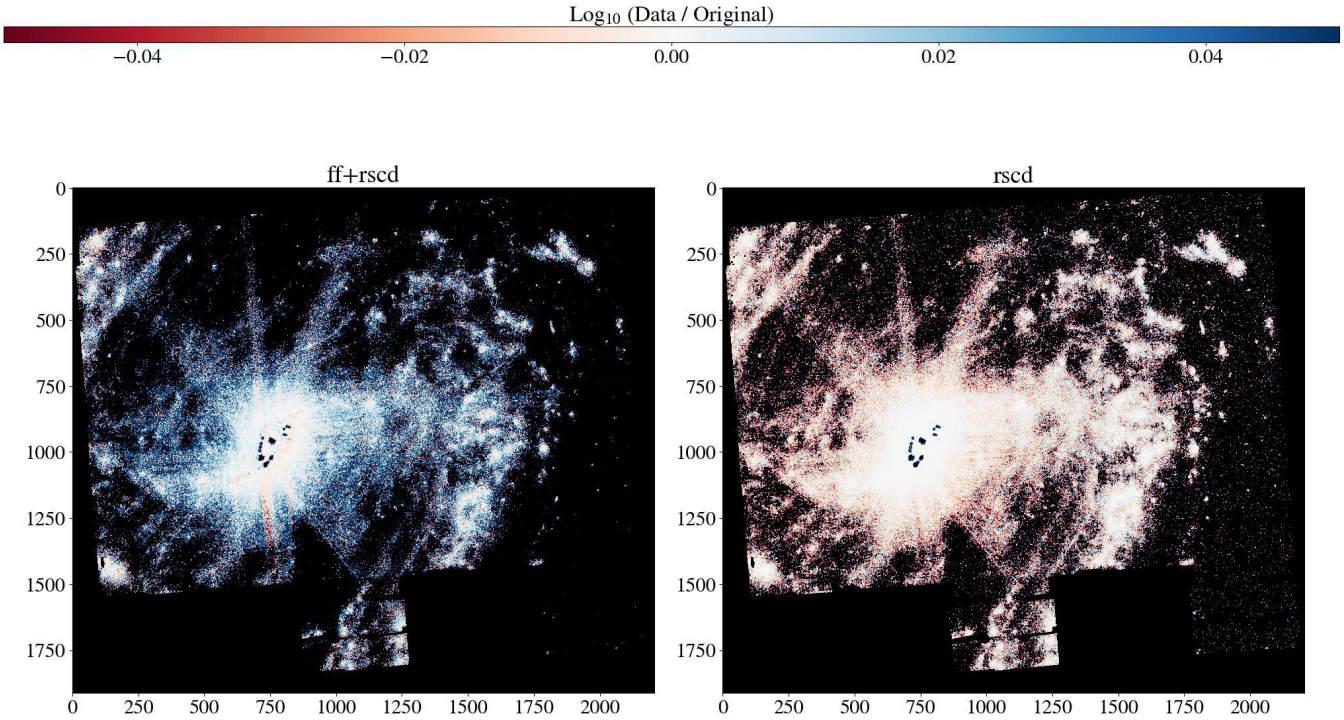

Figure B1. Ratio maps of NGC 1365 (*F2100W*) comparing our saturation-corrected images versus the original pipeline images described in T. G. Williams et al. (2024). On the left, we show the difference between the original map and that which we correct by amending both the first frame and RSCD steps (see Section 2.2), while the right image shows the difference between the original map and that which is corrected by amending only the RSCD step. White represents areas where the original and corrected images are equivalent, while colours represent areas where the corrected pixels are up to ∼10 per cent greater (blue) or lower (red) than the original image. While both corrections do a good job recovering areas with signal, the greater overall coverage of white and light red in the RSCD-only corrected image highlights better consistency with the original image in areas with lower signal. Where there is no signal (background), the differences are stochastic and greater than our scale bar allows, and are hence black. Also, in the centre of the galaxy, the black areas indicate the locations of the saturated regions which undergo significant corrections with the implementation of these steps.

in both of these ratio maps that where there is signal, there are almost no changes compared to the original image, as highlighted by the orange colour. For pixels which originally recorded a flux of at least 5 MJy sr^{-1}, both the mean and median difference for both corrections were less than 0.5 per cent (for reference, all of the sources in our catalogue have fluxes >100 MJy sr^{-1}). This of course excludes the clearly saturated objects themselves which have undergone significant correction. These can be seen as bright yellow spots slightly left of centre in each of the images, where the centre of the galaxy is located.

The biggest difference between the two corrections, however, occurs in the low-end flux regime. As shown in the first-frame + RSCD-corrected ratio map (left panel of Fig. B1), there appears to be more structure than in the RSCD-only-corrected image (right panel). In particular, there appears to be a yellow glow towards the edges of the higher signal regions, indicating overestimation of flux as one moves toward the background. The RSCD-only-corrected image, however, shows almost no such effect. Further, the estimation of background pixels appears much more stochastic in the left panel versus the right. These effects are further described in Fig. B2, which detail the pixel-by-pixel variations for each of the corrected images for pixels which have fluxes under 10 MJy sr^{-1}. In this flux region, the first frame + RSCD-corrected image introduces over twice the scatter as the RSCD-only-corrected image (0.147 versus 0.67), and at the extreme ends of the plots one can see the first frame + RSCD corrections extend ∼0.5 dex further than the RSCD-only corrections. Lastly, the RSCD-corrected image preserves the PSFs of sources much better than the first frame + RSCD-corrected image. An example of this is highlighted in Fig. B3, where the first-frame + RSCD-corrected image appears to artificially smooth the PSF, resulting in an FWHM ∼2 pixels greater than the original image. With these comparisons in mind, we employ the use of the RSCD-only corrected images for the photometry of our sample of SF regions.

Other works have explored the use of fitting an outer PSF in order to recover the photometry of saturated sources (e.g. D. Liu et al. 2023). While this may be viable for a small number of sources, we focus our attention in this work's analysis on the greater sample of objects we have at our disposal.

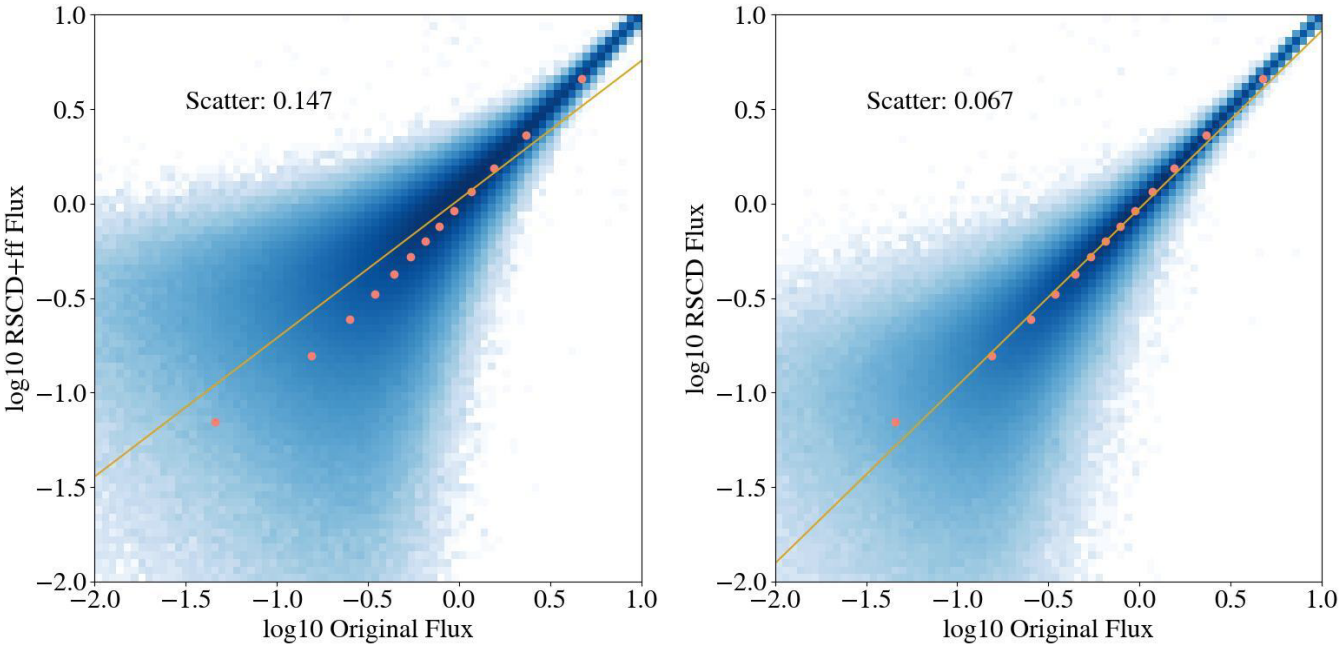

Figure B2. Comparison of pixel values in *F2100W* for our saturation-corrected images versus the pixels from the original pipeline images described in T. G. Williams et al. (2024). On the left, we show the difference between the original pixels and those which we correct by amending both the first frame and RSCD steps (see Section 2.2), while the right image shows the difference between the original pixels and those corrected by amending only the RSCD step. Orange points represent binned medians while the orange line shows a simple least-squares fit for each distribution. Both corrections appear to well-match the original pixel values as long as there is reasonable signal (i.e. more than a few MJy/sr – all of the sources in our catalogue have pixel values of at least, and often much greater than, 100 MJy sr^{-1}). However as we highlight in these diagrams, when we look at the low-end flux regime, the first frame + RSCD-corrected images introduce more scatter compared to the RSCD-only-amended image. Additionally, the first frame + RSCD-corrected images show slightly sublinear differences in this low-end flux regime, while the RSCD-only-corrected image remains linear in its differences.

APPENDIX C: SED MODELLING

The SED modelling presented in the main body of this work utilizes the BC03 SSP models (G. Bruzual & S. Charlot 2003). In addition to the results of the SED fitting we have shown, we have also thoroughly examined the use of an alternative SSP model from Charlot & Bruzual (CB19; A. Plat et al. 2019), as well as modifications to the grid of parameters used for fitting. CB19 represents the latest major revision of the BC03 models, replacing the Padova isochrones with PARSEC stellar evolutionary tracks (A. Bressan et al. 2012), which incorporate updated models for the physics of TP-AGB stars (P. Marigo et al. 2013) and stellar winds from massive stars (Y. Chen et al. 2015).

Overall, we find that the CB19 models do not appear to be well-suited for our specific use case. Keeping all other parameters the same as the BC03 models we have presented, the main difference we see in the CB19 model SEDs for young SF regions across our wavelength range is that the optical slope appears relatively flattened, whereas the slope and features across the NIR and MIR are nearly identical to the BC03 models. As a result, the models appear to push nearly our entire sample of SF regions to the youngest ages (∼1 Myr) to match the optical slopes we observe from our photometry, while the optical SED model of, for example, a 3 Myr source with $E(B-V) = 1$ mag is nearly flat. This collapse of ages to 1 Myr with the CB19 models is consistent across many iterations of fitting, which has included modifications to the dust attenuation model used, the dust emission model (e.g. mass fraction of PAHs, interstellar radiation field parameters), as well as more expansive age grids (out to 13.7 Gyr) and $E(B-V)$ grids (up to 10 mag). This is likely related to our specific analysis, which convolves our images to 0.67 arcsec and thus includes emission from the immediate surroundings of clusters in their photometry.

With the CB19 models, we find optically visible SF regions without H$\,\alpha$ emission also pushed to these very young ages, and nearly all of the age-distinguishing features, which we have discussed in this work and have been shown in others to be reliable (e.g. K. M. Sandstrom et al. 2023; K. F. Henny et al. 2025), are effectively wiped out. Thus we determine that, at least for our analysis of sources convolved to 0.67 arcsec, the BC03 models are more reliable in providing relatively accurate results, despite the older-than-expected absolute ages.

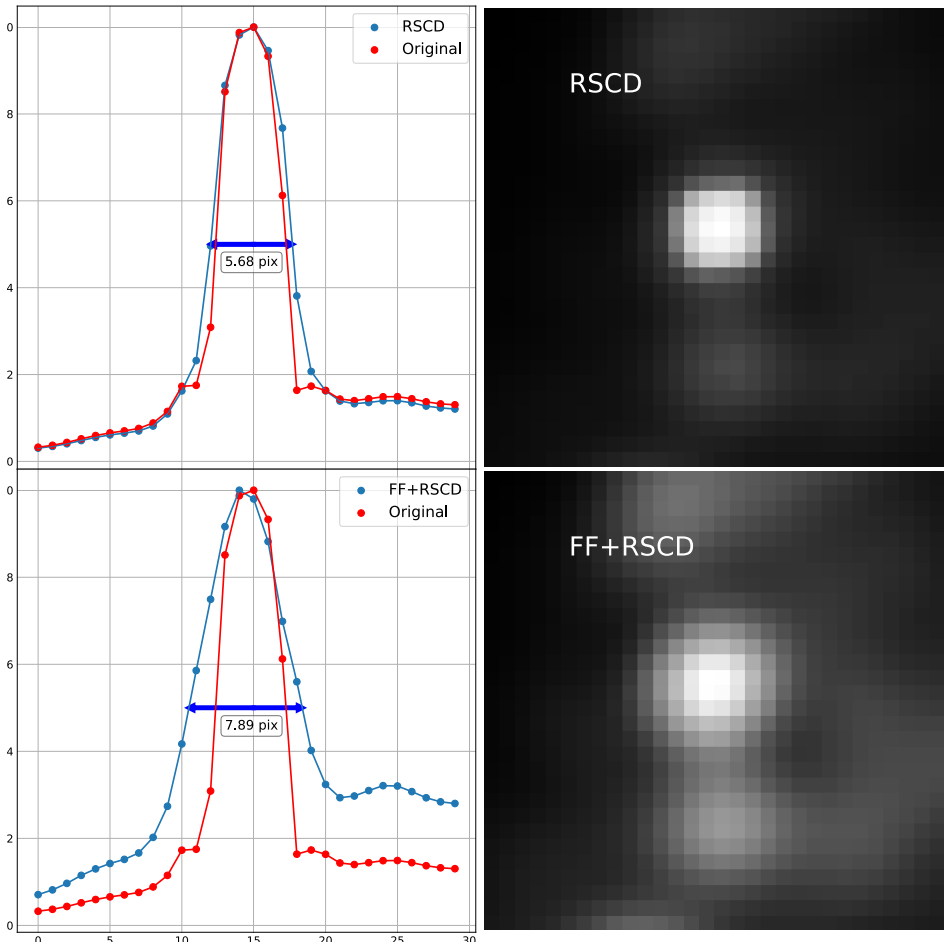

Figure B3. SFs of a slowly saturated source (see Fig. 4) before and after saturation corrections. On the left, we show the normalized flux across this source, where the blue and red lines indicate the 21 μm flux from the corrected and original images, respectively. The result from the first frame + RSCD-corrected image is a smoothing effect, which is also visible in the corresponding MIRI/F2100W image on the right, such that the FWHM of the source is over 2 pixels greater than that of the original image. Comparatively, the RSCD-corrected image on the top row matches much more closely with the original PSF.

APPENDIX D: RESULTS OF SED FITTING

The statistical properties of the SF regions as determined by the SED fitting are summarized in Table D1 for objects that are only identified in one of the original source catalogues. The individual SEDs for all SF regions used for fitting, separated by their detection bands, are shown in Fig. D1.

Table D1. Statistical properties of star clusters as determined by our SED fitting. This table shows the properties of clusters which are only identified in one of the original source catalogues, while Table 2 allows sources which are identified in multiple catalogues to be included in the statistics of each sample, and we find general agreement in the trends between the two. Median SED ages, $E(B-V)$s, masses, and goodness of fit (as measured by the reduced χ^2), along with the standard deviation and [25th, 75th] percentiles are provided for each sample.

SED Estimate	Age (Myr)	$E(B-V)$	Mass (10^5 $M_\odot$)
HST & PAH	9.2 + /− 4.9 [5.2, 11.4]	0.94 + /− 0.42 [0.83, 1.54]	5.4 + /− 5.7 [2.8, 14]
10μm	4.4 + /− 4.5 [3.0, 5.0]	1.32 + /− 0.73 [1.00, 1.54]	7.9 + /− 9.1 [2.9, 17]
21μm	5.6 + /− 2.9 [4.9, 7.6]	1.62 + /− 0.33 [1.32, 2.00]	2.4 + /− 2.6 [1.0, 4.1]
ALMA	5.1 + /− 3.2 [2.0, 8.1]	1.21 + /− 0.56 [1.02, 1.53]	3.8 + /− 3.6 [1.5, 5.6]

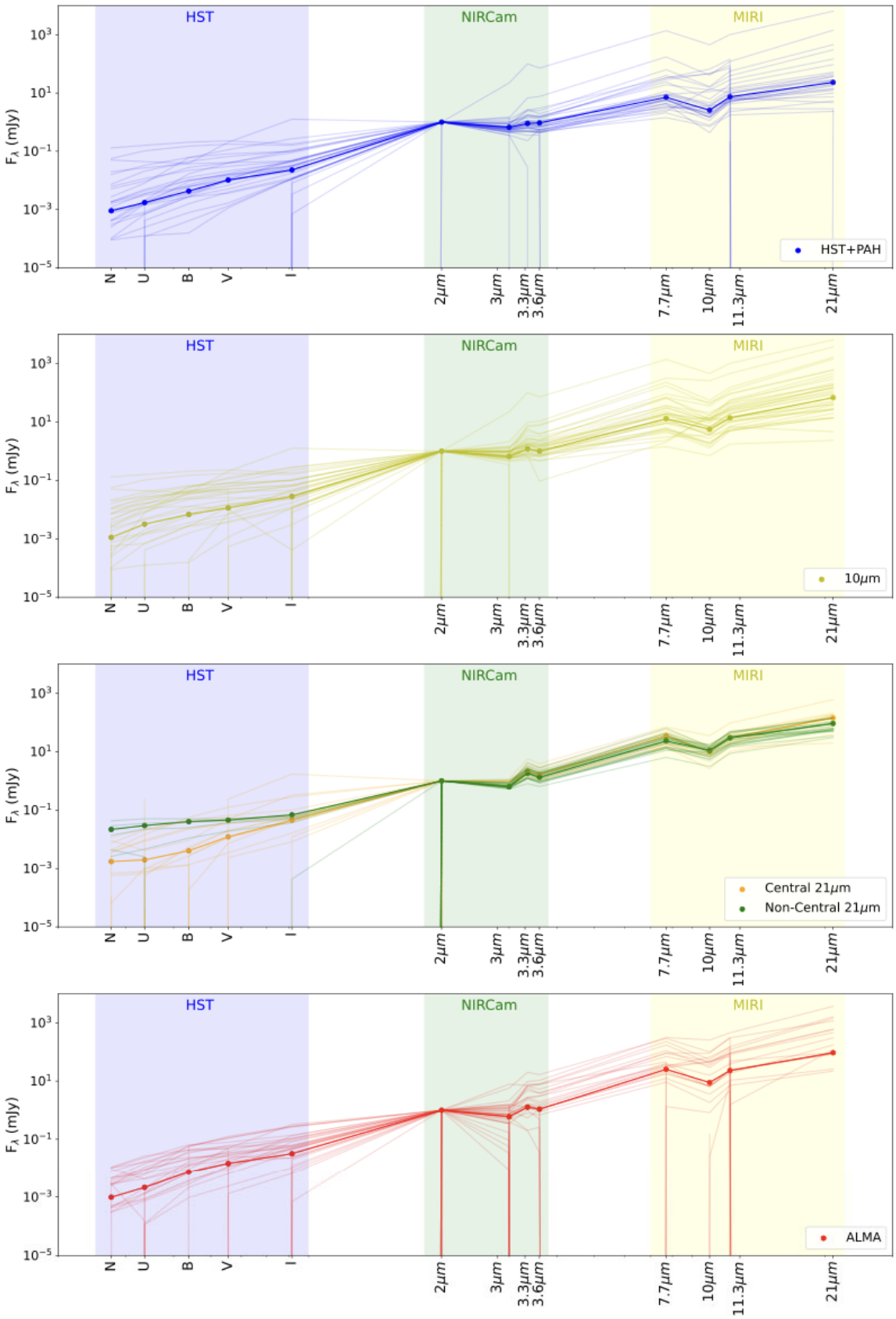

Figure D1. SEDs of SF regions in NGC 1365, split up by the method by which they were identified. All fluxes have been normalized to the flux from NIRCam/F200W. The darker line and points in each plot indicate the median SED of all objects identified in that particular catalogue.

[1]*Max – Planck – Institut für Astronomie, Königstuhl 17, D-69117 Heidelberg, Germany*
[2]*Space Telescope Science Institute, 3700 San Martin Drive, Baltimore, MD 21218, USA*
[3]*Dept. of Physics, University of Alberta, 4-183 CCIS, Edmonton, Alberta T6G 2E1, Canada*
[4]*Purple Mountain Observatory, Chinese Academy of Sciences, 10 Yuanhua Road, Nanjing 210023, China*
[5]*Department of Physics and Astronomy, The Johns Hopkins University, Baltimore, MD 21218, USA*
[6]*Whitman College, 345 Boyer Avenue, Walla Walla, WA 99362, USA*
[7]*Steward Observatory, University of Arizona, Tucson, AZ 85721, USA*
[8]*Instituto de Astrofisica de La Plata, CONICET–UNLP, Paseo del Bosque S/N, B1900FWA La Plata, Argentina*
[9]*Sub-department of Astrophysics, Department of Physics, University of Oxford, Keble Road, Oxford OX1 3RH, UK*
[10]*Université Côte d'Azur, Observatoire de la Côte d'Azur, CNRS, Laboratoire Lagrange, F-06000 Nice, France*
[11]*Department of Physics and Astronomy, University of Wyoming, Laramie, WY 82071, USA*
[12]*Universität Heidelberg, Zentrum für Astronomie, Institut für theoretische Astrophysik, Albert-Ueberle Str. 2, D-69120 Heidelberg, Germany*
[13]*Universität Heidelberg, Interdisziplinäres Zentrum für wissenschaftliches Rechnen, Im Neuenheimer Feld 205, D-69120 Heidelberg, Germany*
[14]*Instituto de Astronomía, Universidad Nacional Autónoma de México, Unidad Académica en Ensenada, Km 103 Carr. Tijuana-Ensenada, Ensenada, BC, C.P. 22860, México*
[15]*Department of Astronomy and Astrophysics, University of California, San Diego, 9500 Gilman Drive, La Jolla, CA 92093, USA*
[16]*ARC Centre of Excellence for All Sky Astrophysics in 3 Dimensions (ASTRO 3D), Canberra, ACT 2611Australia*
[17]*Research School of Astronomy and Astrophysics, Australian National University, Canberra, ACT 2611, Australia*
[18]*Department of Astronomy, University of Virginia, 530 McCormick Road, Charlottesville, VA 22904, USA*
[19]*National Radio Astronomy Observatory, 520 Edgemont Road, Charlottesville, VA 22903, USA*
[20]*Astronomisches Rechen-Institut, Zentrum für Astronomie der Universität Heidelberg, Mönchhofstr. 12-14, D-69120 Heidelberg, Germany*

This paper has been typeset from a TEX/LATEX file prepared by the author.